UNIVERSITY OF COPENHAGEN

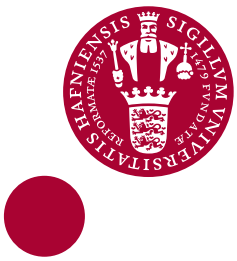

Asymptotically Stable Numerical Method for Multispecies Momentum Transfer Gas and Multifluid Dust Test Suite and Implementation in FARGO3D

Benitez-Llambay, Pablo; Krapp, Leonardo; Pessah, Martin E.

Published in:
Astrophysical Journal Supplement Series

DOI:
10.3847/1538-4365/ab0a0e

Publication date:
2019

Document version
Publisher's PDF, also known as Version of record

Document license:
CC BY-NC

Citation for published version (APA):
Benitez-Llambay, P., Krapp, L., & Pessah, M. E. (2019). Asymptotically Stable Numerical Method for Multispecies Momentum Transfer: Gas and Multifluid Dust Test Suite and Implementation in FARGO3D. *Astrophysical Journal Supplement Series*, *241*(2), [25]. https://doi.org/10.3847/1538-4365/ab0a0e

Download date: 05. maj. 2023

The Astrophysical Journal Supplement Series, 241:25 (22pp), 2019 April https://doi.org/10.3847/1538-4365/ab0a0e
© 2019. The American Astronomical Society. All rights reserved.

Asymptotically Stable Numerical Method for Multispecies Momentum Transfer: Gas and Multifluid Dust Test Suite and Implementation in FARGO3D

Pablo Benítez-Llambay, Leonardo Krapp, and Martin E. Pessah
Niels Bohr International Academy, Niels Bohr Institute, Blegdamsvej 17, DK-2100 Copenhagen Ø, Denmark; pbllambay@nbi.ku.dk, krapp@nbi.ku.dk
Received 2018 November 19; revised 2019 February 7; accepted 2019 February 21; published 2019 April 1

Abstract

We present an asymptotically and unconditionally stable numerical method to account for the momentum transfer between multiple species. Momentum is conserved to machine precision. This implies that the asymptotic equilibrium corresponds to the velocity of the center of mass. Aimed at studying dust dynamics, we implement this numerical method in the publicly available code FARGO3D. To validate our implementation, we develop a test suite for an arbitrary number of species, based on analytical or exact solutions of problems related to perfect damping, damped sound waves, shocks, local and global gas–dust radial drift in a disk, and linear streaming instability. In particular, we obtain first-order steady-state solutions for the radial drift of multiple dust species in protoplanetary disks (PPDs), in which the pressure gradient is not necessarily small. We additionally present nonlinear shearing-box simulations of the streaming instability and compare them with previous results obtained with Lagrangian particles. We successfully validate our implementation by recovering the solutions from the test suite to second- and first-order accuracy in space and time, respectively. From this, we conclude that our scheme is suitable, and very robust, to study the self-consistent dynamics of several fluids. In particular, it can be used for solving the collisions between gas and dust in PPDs, with any degree of coupling.

Key words: circumstellar matter – hydrodynamics – methods: numerical – planets and satellites: formation – protoplanetary disks

1. Introduction

Protoplanetary disks (PPDs) are composed of a collection of gases and dust grains orbiting a young star. In general, the dynamics of this mixture is complex, and self-consistent calculations—including the coupling between different species—are required to produce sensible models. In addition, there is little doubt that self-consistent dust evolution is necessary to correctly interpret observations of PPDs.

Unperturbed gaseous disks rotate at a sub-Keplerian speed because of the pressure gradient. However, dust particles are pressureless, so they tend to move at Keplerian speed. This mismatch between the gas and dust velocities results in a headwind that exchanges momentum and energy between the species. When considering an unperturbed disk formed by one gas and one dust species, Whipple (1972) and Weidenschilling (1977) showed that the dust species drifts inwards, spiraling toward the central star. Momentum conservation makes the gas rotate slightly faster, but because the dust-to-gas mass ratio is usually small, gas dynamics is mostly unaffected. However, under some circumstances, local dust concentrations in the disk can modify the gas dynamics significantly. For example, dust can accumulate in vortices in transitional disks (e.g., Barge & Sommeria 1995; Lyra & Lin 2013; Zhu & Stone 2014; Ragusa et al. 2017), in lopsided disks (Baruteau & Zhu 2016), and at the edges of planet-carved gaps (e.g., Dipierro & Laibe 2017; Weber et al. 2018). Dust can also concentrate due to torques exerted by low-mass planets (e.g., Benítez-Llambay & Pessah 2018; Chen & Lin 2018). It has also been shown that dust can concentrate because of vortices induced by the self-organization due to the Hall effect in magnetized disks (e.g., Béthune et al. 2016; Krapp et al. 2018), among many others mechanisms.

Because of the importance of dust dynamics in PPDs, several tools have been developed to study this problem numerically (e.g., Johansen et al. 2004; Fromang & Papaloizou 2006; Paardekooper & Mellema 2006; Youdin & Johansen 2007; Balsara et al. 2009; Bai & Stone 2010; Hanasz et al. 2010; Miniati 2010; Laibe & Price 2012, 2014; Baruteau & Zhu 2016; Yang & Johansen 2016; Chen & Lin 2018; Hutchison et al. 2018; Price et al. 2018; Riols & Lesur 2018; Stoyanovskaya et al. 2018).

Two different approaches are usually followed when solving the dynamics of dust embedded in a gaseous medium. Dust is usually modeled either as Lagrangian particles or as a pressureless fluid. For example, Lagrangian particles are used in the public codes PIERNIK (Drążkowska et al. 2010; Hanasz et al. 2010), PENCIL (Brandenburg & Dobler 2002; Yang & Johansen 2016), ATHENA (Stone et al. 2008; Bai & Stone 2010), and PHANTOM (Price et al. 2018). A smaller number of examples can be found treating dust as a pressureless fluid, for example, PIERNIK (e.g., Kowalik et al. 2013), FARGO_THORIN (Chrenko et al. 2017), and MPI-AMRVAC (Porth et al. 2014).

To our knowledge, only two implementations are able to solve the dynamics of multiple fluids: PIERNIK and MPI-AMRVAC. Neither of these codes is able to exploit the computing power of graphics processing units (GPUs), which have proven to be an excellent tool for solving PPD-related problems (e.g., Fung et al. 2014; Benítez-Llambay & Masset 2016).

In this paper, we present a numerical method to solve the momentum transfer between multiple species in a precise and stable manner. We show that the implementation of this method in the publicly available GPU code FARGO3D (Benítez-Llambay & Masset 2016) correctly describes the self-consistent dynamics of a mixture of gas and multiple pressureless dust species.

The goals of this paper are (i) to comprehensively describe the numerical method together with its most important properties, (ii) to develop a test suite for an arbitrary number of fluid species, and (iii) to validate our implementation in FARGO3D, not only by recovering the solutions of the test suite but also by studying the numerical convergence.

This paper is organized as follows: in Section 2, we present and discuss the properties of the numerical method used to solve the momentum transfer between multiple species and its implementation in FARGO3D. In Section 3, we present a test suite and compare the obtained analytical or exact solutions with those resulting from our implementation. In this section, we additionally show results of the nonlinear evolution of the two-fluid streaming instability. Finally, in Section 4 we discuss the main results and perspectives of this work.

2. Numerical Scheme

To present our implementation, we consider a set of N species in which the temperature depends on the spatial coordinates only. In this work, we furthermore ignore the possibility of mass transfer between different species, which can be important in, for instance, dust coagulation processes or chemical reactions (see Appendix A for a discussion about this implementation). We do not consider viscous or external body forces, whose implementation has been presented in Benítez-Llambay & Masset (2016). Under these assumptions, the dynamics of the system is completely described by the continuity and Euler equations for each species, which contain an additional term accounting for the momentum transfer between them (e.g., Braginskii 1965; Benilov 1997). Labeling the density and velocity by ρ and $\boldsymbol{v}$, respectively, the equations describing the N-species system are

$$\frac{D\rho_i}{Dt} = -\rho_i \nabla \cdot \boldsymbol{v}_i, \tag{1}$$

$$\frac{D\boldsymbol{v}_i}{Dt} = -\frac{\nabla P_i}{\rho_i} + \frac{\boldsymbol{F}_i}{\rho_i}, \tag{2}$$

with $i = 1, \cdots, N$ being an index referring to each species, $D/Dt = \partial/\partial_t + \boldsymbol{v} \cdot \nabla \boldsymbol{v}$ is the material derivative, and ρ_i is the pressure associated with the ith species. The drag force per unit volume, $\boldsymbol{F}_i$, is defined as

$$\boldsymbol{F}_i = -\rho_i \sum_{j \neq i} \alpha_{ij} (\boldsymbol{v}_i - \boldsymbol{v}_j), \tag{3}$$

with α_{ij} the collision rate between species i and j. This collision rate parameterizes the momentum transfer per unit time and is, in general, a function of the physical properties of the species and their mutual relative velocity. Momentum conservation implies

$$\rho_i \alpha_{ij} = \rho_j \alpha_{ji}. \tag{4}$$

2.1. Implicit Update

We solve the $4N$ equations described by Equations (1) and (2) in the framework of the operator-splitting approximation (e.g., Hawley et al. 1984; Stone & Norman 1992). In this formalism, each equation is usually split into two, (i) the transport step and (ii) the source step (see, e.g., Stone & Norman 1992; Benítez-Llambay & Masset 2016). In our implementation, the collision terms are solved as a new substep within the source step (see Section 2.4 for more details). In this approximation, the additional equation that needs to be solved is[1]

$$\frac{\partial \boldsymbol{v}_i}{\partial t} = \frac{\boldsymbol{F}_i}{\rho_i}. \tag{5}$$

In FARGO3D, the source step is solved using explicit updates. However, a very restrictive stability condition appears when solving a mixture of multiple fluids explicitly (see, e.g., Stoyanovskaya et al. 2018; Vorobyov et al. 2018). In this case, the time step becomes small for large collision rates. Thus, it is convenient to adopt an implicit scheme to solve Equation (5). The most straightforward formula is obtained by expressing this equation in finite differences and evaluating the velocities on the right-hand side in the advanced time, i.e.,

$$\frac{\boldsymbol{v}_i^{n+1} - \boldsymbol{v}_i^n}{\Delta t} = -\sum_{j \neq i} \alpha_{ij}^n (\boldsymbol{v}_i^{n+1} - \boldsymbol{v}_j^{n+1}). \tag{6}$$

Equation (6) corresponds to a set of $3N$ linear algebraic equations for the unknown $\boldsymbol{v}^{n+1}$ velocities, which can be written in a more convenient way as

$$\boldsymbol{v}_i^{n+1}\left[1 + \Delta t \sum_{j \neq i} \alpha_{ij}^n\right] - \Delta t \sum_{j \neq i} \alpha_{ij}^n \boldsymbol{v}_j^{n+1} = \boldsymbol{v}_i^n. \tag{7}$$

A compact form of Equation (7) is obtained by defining the column vectors

$$\boldsymbol{V}_k = [\, \boldsymbol{v}_1 \cdot \boldsymbol{e}_k, \;\; ..., \boldsymbol{v}_N \cdot \boldsymbol{e}_k \,]^{\intercal}, \tag{8}$$

that is, $\boldsymbol{V}_k$ is formed by the projection of the velocity of each species along the direction of the unit vector $\boldsymbol{e}_k$, with $k = 1, 2, 3$. The superscript $\intercal$ stands for transpose. This makes it possible to write Equation (7) as the matrix equation

$$\boldsymbol{T}\boldsymbol{V}_k^{n+1} = \boldsymbol{V}_k^n, \tag{9}$$

where

$$\boldsymbol{T} = \boldsymbol{I} + \Delta t \boldsymbol{M} \tag{10}$$

is an $N \times N$ matrix, $\boldsymbol{I}$ is the identity matrix, and the (i, j) element of the matrix $\boldsymbol{M}$ is

$$\boldsymbol{M}_{ij} \equiv \sum_{k \neq i}^{N} \alpha_{ik}^n \delta_{ij} - \alpha_{ij}^n (1 - \delta_{ij}). \tag{11}$$

The first and second terms in Equation (11) set the diagonal and nondiagonal elements of $\boldsymbol{M}$, respectively. Because $\boldsymbol{T}$ is nonsingular (see Appendix B.1), the solution of Equation (9) exists.

Stone (1997) showed a simple solution of Equation (9) for two species. However, the complexity of these solutions rapidly increases with N, making them impractical. In this paper, we solve Equation (9) numerically by means of Gaussian elimination with partial pivoting (see, e.g., Press et al. 2007, Chapter 2).

[1] It is worth noticing that the method presented in this work holds in the Lagrangian formalism when, in Equation (5), the partial time derivative is replaced by the material one.

2.2. Properties of the Implicit Scheme

Two important properties of the method arise from Equation (9). These are momentum conservation to machine precision and asymptotic stability for any Δt.

2.2.1. Momentum Conservation to Machine Precision

The implicit scheme, defined by Equation (9), conserves total momentum to machine precision. This property can be demonstrated by comparing the momentum before and after the application of the operator $\boldsymbol{T}$.

We first calculate the momentum of the system at time t_n and write the old velocities in terms of the new ones via Equation (9). Defining $a_{ij} = \Delta t \alpha_{ij}^n$, it follows that

$$\begin{aligned}
&\sum_i \rho_i \boldsymbol{v}_i^n \\
&= \sum_i \rho_i \sum_j \left[\left(1 + \sum_{k\neq i} a_{ik} \right) \delta_{ij} - a_{ij}(1-\delta_{ij}) \right] \boldsymbol{v}_j^{n+1} \\
&= \sum_j \boldsymbol{v}_j^{n+1} \sum_i \rho_i \left[\left(1 + \sum_{k\neq i} a_{ik} \right) \delta_{ij} - a_{ij}(1-\delta_{ij}) \right] \\
&= \sum_j \boldsymbol{v}_j^{n+1} \left[\rho_j + \rho_j \sum_{k\neq i} a_{jk} - \sum_{i\neq j} \rho_i \frac{\rho_j}{\rho_i} a_{ji} \right] \\
&= \sum_j \boldsymbol{v}_j^{n+1} \rho_j \left[1 + \sum_{k\neq i} (a_{jk} - a_{jk}) \right] \\
&= \sum_j \rho_j \boldsymbol{v}_j^{n+1}, \qquad (12)
\end{aligned}$$

where we have used condition (4) and replaced i by k in the last step. In this calculation, the densities are evaluated at time t_n because the collision step does not modify them. We thus conclude that

$$\sum_i \rho_i \boldsymbol{v}_i^{n+1} = \sum_i \rho_i \boldsymbol{v}_i^n \;=\; \ldots \;=\; \sum_i \rho_i \boldsymbol{v}_i^0, \qquad (13)$$

implying that the implicit scheme conserves momentum to machine precision.

2.2.2. Asymptotic Stability

The implicit scheme defined by Equation (9) is asymptotically stable. That is,

$$\lim_{n\to\infty} \boldsymbol{T}^{-n} \boldsymbol{V}_k^0 - \boldsymbol{c} = 0 \qquad (14)$$

for some constant vector $\boldsymbol{c}$ and any vector $\boldsymbol{V}_k^0$. To prove this property, we use the fact that $\boldsymbol{T}^{-1}$ is a right stochastic and strictly positive matrix (see Appendices B.3 and B.4). Hence, from the Perron–Frobenius theorem, $\boldsymbol{T}^{-1}$ converges to a matrix with identical rows, i.e.,

$$\lim_{n\to\infty} (\boldsymbol{T}^{-n})_{ij} = p_j, \qquad (15)$$

where p_j is the jth element of a vector $\boldsymbol{p}$. In the following, we only use the fact that $\boldsymbol{p}$ is a constant vector.

By definition, for any direction $\boldsymbol{e}_k$, the implicit scheme satisfies

$$\boldsymbol{V}_k^{n+1} = \boldsymbol{T}^{-1} \boldsymbol{V}_k^n \;=\; \cdots \;=\; \boldsymbol{T}^{-(n+1)} \boldsymbol{V}_k^0. \qquad (16)$$

It then follows that the asymptotic limit is

$$\lim_{n\to\infty} \boldsymbol{V}_k^{n+1} = \lim_{n\to\infty} \boldsymbol{T}^{-(n+1)} \boldsymbol{V}_k^0 \equiv V_{\mathrm{c},k} \mathbb{1}^{\mathsf{T}}, \qquad (17)$$

where $\mathbb{1}^{\mathsf{T}}$ is a vector whose elements are all equal to one and $V_{\mathrm{c},k} = \boldsymbol{p} \cdot \boldsymbol{V}_k^0$. Because momentum is conserved, it follows that

$$V_{\mathrm{c},k} \sum_{j=1}^{N} \rho_j = \sum_{j=1}^{N} \rho_j V_{jk}^0, \qquad (18)$$

from which we prove that the asymptotic limit (17) corresponds to the velocity of the center of mass, $V_{\mathrm{CM},k}$, defined as

$$V_{\mathrm{CM},k} = \frac{\sum_{j=1}^{N} \rho_j V_{jk}^0}{\sum_{j=1}^{N} \rho_j}. \qquad (19)$$

Thus, we conclude that the numerical method converges asymptotically to the velocity of the center of mass, and this is independent of the choice of Δt.

Now, we address the problem of the stability and convergence for any sufficiently large time step, that is

$$\lim_{\Delta t\to\infty} \boldsymbol{T}^{-1} \boldsymbol{V}_k^n - \boldsymbol{d} = 0, \qquad (20)$$

for some constant vector $\boldsymbol{d}$ and any vector $\boldsymbol{V}_k^n$. In Appendix B.2, we show that $\boldsymbol{T}^{-1}$ is diagonalizable, with diagonal form

$$\boldsymbol{\Lambda}_{ij} = \frac{1}{1 + \Delta t \lambda_{Mi}} \delta_{ij}, \qquad (21)$$

where λ_{Mi} are the eigenvalues of $\boldsymbol{M}$, with $\lambda_{Mj} = 0$ for some j. Because $\boldsymbol{T}^{-1}$ is right stochastic, $\lambda_{Mj} = 0$ has algebraic multiplicity equal to one. Thus, for any sufficiently large time step, all the entries of $\boldsymbol{\Lambda}$ approach zero, except $\Lambda_{jj} = 1$. Then, Equation (9) can be decoupled, and it adopts the form

$$\hat{\boldsymbol{V}}_k^{n+1} = \boldsymbol{\Lambda} \hat{\boldsymbol{V}}_k^n, \qquad (22)$$

where $\hat{\boldsymbol{V}}_k = \boldsymbol{P}^{-1} \boldsymbol{V}_k$, with $\boldsymbol{P}$ the matrix whose columns are the eigenvectors of $\boldsymbol{T}^{-1}$. In the limit of large Δt, Equation (22) reads

$$\lim_{\Delta t\to\infty} (\hat{\boldsymbol{V}}_k)_i^{n+1} = \hat{V}_{j,k}^n \delta_{ij}. \qquad (23)$$

Because we set $\Lambda_{jj} = 1$ and $\boldsymbol{T}^{-1}$ is right stochastic, all the entries of the column $\boldsymbol{P}_j$ are equal to one, that is, $\boldsymbol{P}_j = \mathbb{1}^{\mathsf{T}}$. We thus obtain

$$\lim_{\Delta t\to\infty} \boldsymbol{V}_k^{n+1} = \lim_{\Delta t\to\infty} \boldsymbol{P} \hat{\boldsymbol{V}}_k^{n+1} = \hat{V}_{j,k}^n \boldsymbol{P}_j = \hat{V}_{j,k}^n \mathbb{1}^{\mathsf{T}}, \qquad (24)$$

which is equivalent to Equation (17).

Equations (17) and (24) allow us to conclude

$$\lim_{n\to\infty} \boldsymbol{T}^{-n} \boldsymbol{V}_k^0 = \lim_{\Delta t\to\infty} \boldsymbol{T}^{-1} \boldsymbol{V}_k^n = V_{\mathrm{CM}} \mathbb{1}^{\mathsf{T}}, \qquad (25)$$

and the implicit scheme is thus asymptotically and unconditionally stable.

2.3. Dust as a Pressureless Fluid

In the case of a system composed of gas and several dust species, dust can be modeled as a pressureless fluid. It is clear that this approximation fails in describing the dynamics of

systems dominated by crossing trajectories, a regime prone to develop when gas and dust species are coupled very weakly.

In our implementation, we ignore collisions between dust species and consider only the interaction between the gas and dust fluids. Thus, dust species interact indirectly between them via their coupling with the gas. Referring to the gas species by the index g, after using condition (4), the collision rate can be written as

$$\alpha_{ij} \equiv \alpha_i \delta_{jg} + \epsilon_j \alpha_j \delta_{gi}, \tag{26}$$

with $\epsilon_j = \rho_j/\rho_g$ and δ_{ig} the Kronecker delta.

In the context of PPDs, the collision rate is usually parameterized via the so-called Stokes number, T_s. It is a dimensionless parameter that characterizes the collision rate in units of the local Keplerian frequency, Ω_K, such that

$$\alpha_i \equiv \frac{\Omega_K}{T_{si}}. \tag{27}$$

The Stokes number depends on the properties of the gas, the dust grains, and their relative velocity (see, e.g., Safronov 1972; Whipple 1972). For simplicity, in this paper, we assume that the Stokes number does not depend on the velocity of the fluid, which has been referred to in the past as the linear drag regime (see Laibe & Price 2011). In what follows, we consider the Stokes number to be constant. Nevertheless, our implementation remains valid when the Stokes number is allowed to vary in space. One example of this is when the dust is characterized by its particle size (see, e.g., Weber et al. 2018). The more general case of a Stokes number depending on the relative velocity is presented in Appendix C.

2.4. Implementation in FARGO3D

We now describe the implementation of the implicit scheme in the code FARGO3D. We first note that the collision term, described by Equation (5), is decoupled from the source and transport substeps. Thus, we evolve every species according to the same algorithms described in Benítez-Llambay & Masset (2016).

The implicit scheme for solving the collision term involves an extra substep, in which the velocity of each species is partially updated according to Equation (9). There are three different options to place this additional partial update: (i) before the source step, (ii) after the source step and before the transport step, or (iii) after the transport step. Options (i) and (iii) are equivalent after the first time step, which we discard because the dust species do not reach the asymptotic limit in the presence of additional forces. In this case, the relative velocity between the dust and gas asymptotes to its terminal velocity, where the additional forces are in balance with the drag forces. Because in options (i) and (iii) the drag forces are computed in the absence of additional forces, they cannot correctly reproduce this limit (Booth et al. 2015). Option (ii) reproduces this limit because evaluating the collision term after the source term is equivalent to a solution treating both terms together.

Although not strictly necessary, the coupling between the source and collision steps can be improved by adding a predictor step before the source step. The source step consists

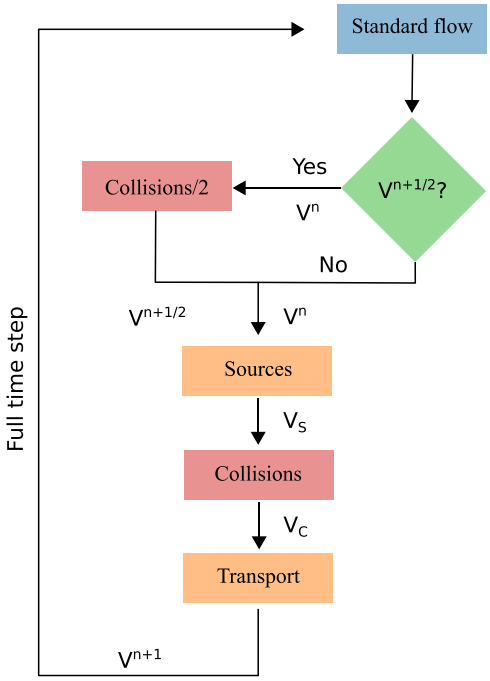

Figure 1. Flowchart of our implementation. During a generic time step Δt, depending on whether the predictor step is required, we call the collision routine using a time step $\Delta t/2$, and obtain a partially updated velocity $V^{n+1/2}$. We then update the velocities by sources and use the output, V_S, as input for the collision step. After this, we use the updated velocities, V_C, as input for the transport step, from which we obtain the updated velocity, V^{n+1}. The flow then returns to the standard flow, from which a full update has been performed.

of a partial update of the form

$$\frac{\partial \boldsymbol{v}}{\partial t} = \mathcal{S}(\boldsymbol{v}), \tag{28}$$

where $\mathcal{S}$ are sources that depend on the velocities. In finite differences, the previous equation reads

$$\boldsymbol{v}^{n+1} = \boldsymbol{v}^n + \Delta t \mathcal{S}(\boldsymbol{v}^*). \tag{29}$$

In the standard implementation, we assume $\boldsymbol{v}^* = \boldsymbol{v}^n$. However, we can improve the coupling between collision and source steps by setting $\boldsymbol{v}^* = \boldsymbol{v}^{n+1/2}$, i.e., by estimating an advanced velocity from the collision step with a time step $\Delta t/2$. We then compute the source step using a full time step and finally calculate the collision step with a full time step. In this paper, we always use the predictor step when the source terms depend on the velocities.

For completeness, in Figure 1 we present a flowchart of our implementation. During a generic time step, depending on whether the predictor step is required, we call the collision routine using a time step $\Delta t/2$ and obtain a partially updated velocity. We then update the velocities of all the species by the standard source terms and use the updated velocities as input for the collision step. During this step, we solve Equation (9) and then use the updated velocities as input for the transport step. After the transport step, a full update has been performed.

3. Numerical Tests

In this section, we present a test suite considering multiple dust species. We use these tests to validate the accuracy, convergence properties, and robustness of the method and

implementation described in Section 2. In all of the following tests, the numerical solutions were obtained using a Courant–Friedrichs–Lewy (CFL) factor of 0.44 (Benítez-Llambay & Masset 2016), unless a different value is specified.

3.1. Time Evolution of a Set of Colliding Species

When a set of N species evolves under the sole effect of the collision term, simple asymptotically convergent analytical solutions can be found. This simple test problem validates the correct implementation of the matrix solver and, at the same time, illustrates the two properties described in the previous section.

As a first step, we show the steady-state solution of the problem, which gives insight into the fundamental property of the physical system, that is, the convergence of all the velocities toward the velocity of the center of mass. In Section 2.2.2, we have already shown that the implicit scheme satisfies this condition.

The steady-state momentum equation for a set of N species when considering only the drag force reduces to the matrix equation

$$\boldsymbol{M}\boldsymbol{V}_k = 0. \tag{30}$$

Because the matrix $\boldsymbol{M}$, defined by Equation (11), is singular (see Appendix B.1), the system (30) admits a nontrivial solution. By direct calculation, it can be shown that the (i, j) element of the echelon form of $\boldsymbol{M}$ is

$$E_{M,ij} = \delta_{ij} - \delta_{jN}. \tag{31}$$

This observation, combined with momentum conservation, allows us to conclude that

$$V_{1k} = \ldots = V_{Nk} = V_{\mathrm{CM},k}, \tag{32}$$

where $V_{\mathrm{CM},k}$ is the velocity of the center of mass, given by Equation (19).

3.1.1. Evolution toward Steady State

We are not only interested in the steady-state solution of the system but also in the time evolution toward this asymptotic steady state. The problem is equally described for any component of the velocity, so it is effectively a collection of 1D problems. Hence, we omit the subscript k.

The temporal evolution of the system is described by the solution of

$$\frac{\partial \boldsymbol{V}}{\partial t} + \boldsymbol{M}\boldsymbol{V} = 0. \tag{33}$$

Without loss of generality, by expressing the solution of Equation (33) as $\boldsymbol{V}(t) = \sum_j \tilde{\boldsymbol{V}}_j e^{-\lambda_j t}$, we reduce Equation (33) to the eigenvalue problem

$$\boldsymbol{M}\tilde{\boldsymbol{V}}_j = \lambda_j \tilde{\boldsymbol{V}}_j. \tag{34}$$

For simplicity, we define the collision rate $\alpha_{ij} \equiv \alpha_0$ for $i > j$ and $\alpha_{ij} = \rho_j/\rho_i \alpha_0$ for $i < j$, such that condition (4) is satisfied.

Defining the function

$$\zeta_j = \sum_{m=j+1}^{N} \rho_m, \tag{35}$$

Table 1
Initial Density, Velocity, Eigenvalues, and Coefficients Needed to Compute the Solution Given by Equation (38)

j	ρ_j	v_j^0	λ_j	c_j
Two fluids				
1	0.2	1.0	0.6000000	−0.8300000
2	1.0	2.0	0.0000000	1.8333333
Three fluids				
1	0.2	1.0	1.5000000	−1.5333333
2	1.0	2.0	0.3800000	−0.6428571
3	1.8	3.0	0.0000000	2.5333333
Six fluids				
1	1.0	−1.0	1.3500000	−0.1925926
2	1.5	2.0	0.9333333	2.7920000
3	2.0	3.1	0.7500000	4.2727273
4	2.5	−2.5	0.6600000	−0.3777778
5	3.0	0.5	0.6166667	2.4769231
6	3.5	−4.1	0.0000000	−0.8074074

Note. In all cases, we set $\alpha_0 = 10^{-1}$.

the eigenvalues of $\boldsymbol{M}$ adopt the expression

$$\lambda_{j<N} = \alpha_0\left(j + \frac{\zeta_j}{\rho_j}\right),$$
$$\lambda_N = 0, \tag{36}$$

with the associated eigenvectors

$$\tilde{\boldsymbol{V}}_{j<N} = \boldsymbol{e}_j - \frac{1}{\zeta_j}\sum_{m=j+1}^{N-1} \rho_{m-1}\boldsymbol{e}_m,$$
$$\tilde{\boldsymbol{V}}_N = \sum_{k=1}^{N} \boldsymbol{e}_k. \tag{37}$$

Thus, the solution reads

$$v_{j<N}(t) = -\sum_{k=1}^{j-1} \frac{\rho_k c_k}{\zeta_k} e^{-\lambda_k t} + c_j e^{-\lambda_j t} + c_N,$$
$$v_N(t) = -\sum_{k=1}^{N-1} \frac{\rho_k c_k}{\zeta_k} e^{-\lambda_k t} + c_N, \tag{38}$$

where the coefficients c_j are

$$c_{j<N} = v_j^0 - V_{\mathrm{CM}} + \sum_{k=1}^{j-1} \frac{\rho_k c_k}{\zeta_k},$$
$$c_N = V_{\mathrm{CM}}. \tag{39}$$

3.1.2. Numerical Solution

We compare the analytical solution found in Section 3.1.1 with that obtained by solving the problem using the implicit scheme. We study the problem with two, three, and six different species. In order to do this, we set the initial condition on a 1D grid with 16 evenly distributed cells, over a periodic domain. We note, however, that this choice is arbitrary and, in practice, irrelevant. This is because the solution does not depend on spatial coordinates. The initial density, velocity, eigenvalues, and coefficients needed to compute both the numerical and analytical solutions for each run are summarized in Table 1. In all cases, we set the collision rate $\alpha_0 = 10^{-1}$.

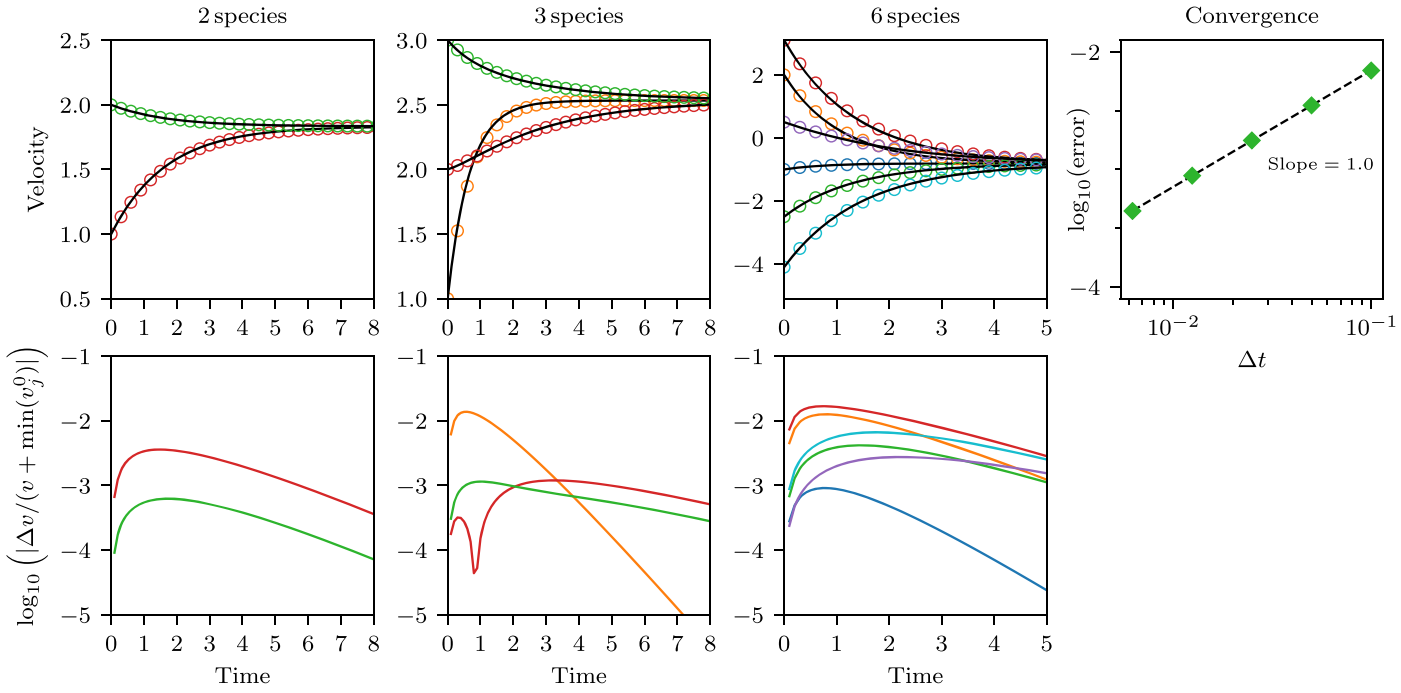

Figure 2. Upper panels: time evolution of the velocity for the various configurations described in Table 1. From left to right, we plot the evolution of two, three, and six species. The solid lines correspond to the analytical solution, given by Equation (38). The unfilled circles were obtained with our implementation, where each color represents a different species. In all panels, the velocities converge to the velocity of the center of mass of the system. Lower panels: time evolution of the relative error between the numerical and the analytical solutions. The color code is the same for the upper and lower panels. The time evolution of the velocities and errors are shown for the run with $\Delta t = 0.1$. In the rightmost panel, we plot, for the case with six species, the error (see Equation (40)) as a function of the time step Δt, for five different time steps.

In the first three panels of Figure 2 (from left to right), we plot, for all species, the time evolution of the velocities. Each panel corresponds to the different configurations listed in Table 1. In the lower panels of Figure 2, we present the relative error of the velocity for all species, for each of the three cases. The time evolution of the error shows the asymptotic convergence demonstrated in Section 2. Independently of the number of species, there is an excellent agreement between the analytical and numerical solutions.

3.1.3. Convergence with Time Step

We additionally check, for the case of six fluids, the expected first-order convergence rate in time of the implicit scheme. For this test, we performed five identical runs, in which we progressively decreased the time step by factors of 2, starting with $\Delta t = 0.1$. In the rightmost panel of Figure 2, we plot the error as a function of the time step, defined as

$$\text{error}(\Delta t) = \left(\sum_{j=1}^{N} \langle v_j^{\Delta t}(t) - v_j(t) \rangle^2 \right)^{1/2}, \tag{40}$$

where $\langle\rangle$ denotes the time average. As expected, the convergence is consistent with a first-order method, i.e., linear convergence with a slope equal to one.

3.2. Damping of a Sound Wave

Sound waves are a natural outcome of the fluid equations when pressure perturbations are considered. Dust fluids, however, cannot support sound waves. In systems composed of gas and dust species, sound waves can propagate—supported by the gas component—but their properties are modified due to the coupling to the gas.

Solutions for the case of one gas and one dust species were found by Laibe & Price (2012), who show that sound waves are damped by the effect of the mutual collision. Solving this problem is relevant because it provides a direct—and perhaps the simplest—way to test the coupling between the implicit solver and the transport and source steps.

In this paper, we derive the dispersion relation for the general problem of one gas and $N - 1$ dust species, which, together with the general expression for the eigenvectors, allow us to find the full solution to the problem.

3.2.1. Dispersion Relation and Eigenvectors

We now derive the dispersion relation for the case of one gas and $N - 1$ dust species and find the general eigenvectors of the problem. For that, we assume that the gas pressure is given by $P = c_s^2 \rho_g$, with a constant sound speed c_s, and define the collision rate between the gas and dust species following Equation (26), with $\alpha_j = t_{sj}^{-1}$, where t_{sj} is the stopping time.

Assuming solutions of the form $\rho_j = \rho_j^0 + \delta\rho_j$ and $v_j = \delta v_j$, with ρ_j^0 constant, and ignoring quadratic terms in the perturbations, the continuity and momentum equations for the

gas and dust species become

$$\frac{\partial \delta\rho_g}{\partial t} + \rho_g^0 \frac{\partial \delta v_g}{\partial x} = 0, \tag{41}$$

$$\frac{\partial \delta\rho_j}{\partial t} + \rho_j^0 \frac{\partial \delta v_j}{\partial x} = 0, \tag{42}$$

$$\frac{\partial \delta v_g}{\partial t} + \sum_{m=1}^{N-1} \frac{\epsilon_m^0}{t_{sm}}(\delta v_g - \delta v_m) + \frac{c_s^2}{\rho_g^0}\frac{\partial \delta\rho_g}{\partial x} = 0, \tag{43}$$

$$\frac{\partial \delta v_j}{\partial t} + \frac{1}{t_{sj}}(\delta v_j - \delta v_g) = 0, \tag{44}$$

where $j = 1, ..., N-1$ is the index of the dust species.

We first note that the momentum equation is decoupled from the continuity equation for dust species, so the order of the problem is effectively reduced from $2N$ to $N+1$. Without loss of generality, we write any perturbation δf as $\delta f = \delta\hat{f}\, e^{ikx-\omega t}$, with k a real wavenumber. Thus, from Equations (41)–(44), we obtain the dispersion relation

$$F(\omega, \omega_s) \equiv \omega^2\left(1 + \sum_{m=1}^{N-1}\frac{\epsilon_m}{1-\omega t_{sm}}\right) + \omega_s^2 = 0, \tag{45}$$

with $\omega_s = kc_s$. The singular values $\omega_m = t_{sm}^{-1}$ correspond to $\delta v_g = 0$ and $\delta\rho_g = 0$, and so are not considered.

Finally, the components of the associated eigenvectors are

$$\frac{\delta\hat{v}_g}{c_s} = -i\frac{\omega}{\omega_s}\frac{\delta\hat{\rho}_g}{\rho_g^0}, \tag{46}$$

$$\frac{\delta\hat{v}_j}{c_s} = -i\frac{\omega}{\omega_s}\frac{1}{(1-\omega t_{sj})}\frac{\delta\hat{\rho}_g}{\rho_g^0}, \tag{47}$$

$$\frac{\delta\hat{\rho}_j}{\rho_j^0} = \frac{1}{1-\omega t_{sj}}\frac{\delta\hat{\rho}_g}{\rho_g^0}, \tag{48}$$

for any $\delta\hat{\rho}_g$, which completes the solution of the problem.

Equation (45) can be written as a polynomial equation of degree $N+1$. In Appendix D, we show that at least $N-1$ roots of Equation (45) are real and positive and are thus associated with pure damping. We furthermore identify the intervals in which they can be found. This allows a simple bisection algorithm to be used to find them. We additionally explain how to use Vieta's formulae to find the final two roots, which are, in general, complex. These two complex roots are the most interesting ones because they describe the propagation of damped sound waves.

3.2.2. Numerical Solution

We obtain numerical solutions for the oscillatory damped modes. From the two possible oscillatory modes, we choose only one because the other is the complex conjugate, producing the same solution but propagating in the opposite direction. We do not consider the solutions that correspond to perfect damping because they behave like those studied in Section 3.1.

We study the cases of one gas fluid combined with one and four dust species, respectively. As initial condition, we set a zero background velocity, constant background density ρ_j^0, and perturbations δf, of the form

$$\delta f = A[\mathrm{Re}(\delta\hat{f})\cos(kx) - \mathrm{Im}(\delta\hat{f})\sin(kx)], \tag{49}$$

where A is a small amplitude needed to ensure linearity. We set its value to $10^{-4}c_s$ and $10^{-4}\rho_g^0$ for the velocity and density perturbations, respectively. We adopt $c_s = 1$. The background densities, perturbation amplitudes, stopping times, and complex eigenvalue for each case are listed in Table 2. We consider a domain of size $L = 1$, with spatial coordinate $x \in [0, L]$, split into 10^3 evenly spaced grid cells. We consider the wavenumber $k = 2\pi/L$ and set periodic boundary conditions.

In Figure 3, we plot, for the two configurations considered, the analytical (solid lines) and numerical (open circles) solutions, measured at $x = 0$. The solution corresponding to each species is plotted with a different color. The first column shows the solution obtained for one gas and one dust species, while the second one shows the same for the case of five, one gas and four dust, species. In the upper and lower panels, we plot the normalized velocity, defined as $\delta\hat{v}/(c_sA)$ and the normalized density, defined as $\delta\hat{\rho}/(\rho A)$, respectively. From Figure 3, it is clear that the analytical solution is successfully recovered by our implementation. This test validates the coupling of the drag force in combination with the source and transport steps for a wide range of stopping times.

To study the coupling of the implicit scheme with the transport and source steps in a more challenging situation, we study the damping of a sound wave for a range of stopping times $10^{-4} \leqslant t_s \leqslant 10$ and a fixed time step, such that we test both stiff and non-stiff regimes for the collisions. We consider the two-fluid problem described in Table 2, for different stopping times. We use a domain of size $L = 1$ and 32 cells, which sets a time step $\Delta t = 1.375 \times 10^{-2}$, given by the standard CFL condition of FARGO3D. For stopping times smaller than the time step, the regime becomes more and more stiff. Note that, because of the CFL condition, the degree of stiffness depends on the resolution. We integrate the system until it reaches a final time $t = 10$. We measure the damping rate, $\mathrm{Re}(\omega)$, and the oscillatory frequency, $\mathrm{Im}(\omega)$, by fitting the numerical solutions. In the upper and lower panels of Figure 4, we show the analytical frequency and damping rate, respectively, together with the measurements from our simulations.

Because the error of the implicit scheme converges to zero asymptotically with Δt (see Section 2), for a fixed time step, the smaller the stopping time is, the stiffer the regime is and the faster the errors are damped. Furthermore, the excellent agreement of the oscillatory frequency allows us to conclude that no phase error is introduced by the implicit scheme in the operator-splitting approximation.

3.3. Shock Solution in the Presence of Dust

Lehmann & Wardle (2018) found steady-state shock solutions for a mixture of gas and one dust species. In this paper, we extend one of those solutions to consider an arbitrary number of dust species, which provides a simple and effective way to test the response of the dust species in the presence of a shock in the gas component. This generalization allows us to test the collision module in combination with the hydro solver in a challenging regime, in which a steady-state solution must be achieved but is not, in principle, numerically guaranteed. Additionally, this test problem allows us to measure how many

Table 2
Initial Conditions for the Damping of the Sound Wave Test

j	ρ_j	$\delta\hat{\rho}_j$	$\delta\hat{v}_j$	t_{sj}	ω
Two species					
g	1.000000	1.000000	$-0.701960 - 0.304924i$	⋯	$1.915896 - 4.410541i$
1	2.240000	$0.165251 - 1.247801i$	$-0.221645 + 0.368534i$	0.4	⋯
Five species					
g	1.000000	1.000000	$-0.874365 - 0.145215i$	⋯	$0.912414 - 5.493800i$
1	0.100000	$0.080588 - 0.048719i$	$-0.775380 + 0.308952i$	0.100000	⋯
2	0.233333	$0.091607 - 0.134955i$	$-0.427268 + 0.448704i$	0.215443	⋯
3	0.366667	$0.030927 - 0.136799i$	$-0.127928 + 0.313967i$	0.464159	⋯
4	0.500000	$0.001451 - 0.090989i$	$-0.028963 + 0.158693i$	1.000000	⋯

cells the shock spreads over in the multiple species configuration.

3.3.1. Generalized Shock Solution for Gas and N Dust Species

The shock solution is obtained after solving the steady-state continuity and momentum equations for the gas and N dust species:

$$\frac{\partial}{\partial x}(\rho_g v_g) = 0, \tag{50}$$

$$\frac{\partial}{\partial x}(\rho_i v_i) = 0, \tag{51}$$

$$\frac{\partial}{\partial x}[\rho_g(v_g^2 + c_s^2)] = -\sum_{i=1}^{N} K_i(v_g - v_i), \tag{52}$$

$$\frac{\partial}{\partial x}(\rho_i v_i^2) = -K_i(v_i - v_g), \tag{53}$$

for $i = 1, \ldots, N$. c_s is the sound speed and, for simplicity, the collision coefficients $K_i \equiv \rho_g \alpha_{gi} = \rho_i \alpha_{ig}$ are assumed to be constant. After integrating Equations (51), we obtain

$$\rho_i v_i = \rho_{i0} v_{i0}, \tag{54}$$

where $\rho_{i0} \equiv \rho_i(x_0)$ and $v_{i0} \equiv v_i(x_0)$, with x_0 an arbitrary coordinate. Defining the velocity $v_s \equiv v_{g0} = v_{10} = \ldots = v_{N0}$, and $\omega_i = v_i/v_s$ and $\omega_g = v_g/v_s$, Equations (53) and (54) lead to the following set of differential equations for the dust velocities:

$$\frac{d\omega_i}{dx} = \frac{K_i}{\rho_{i0} v_{i0}}(\omega_g - \omega_i). \tag{55}$$

The normalized gas velocity is obtained after integrating the sum of Equations (52) and (53). This allows ω_g to be obtained as the root of the quadratic equation

$$\omega_g^2 + \omega_g\left[\sum_{i=1}^{N}\epsilon_i(\omega_i - 1) - \mathcal{M}^{-2} - 1\right] + \mathcal{M}^{-2} = 0, \tag{56}$$

where $\epsilon_i = \rho_{i0}/\rho_{g0}$ is the dust-to-gas mass ratio of each species and $\mathcal{M} = v_s/c_s$ is the Mach number. Equations (55), together with the closed expression for ω_g given by the solution of Equation (56), allow us to find the steady-state normalized velocities as the solution of an initial value problem, described by a set of N coupled first-order differential equations, with the initial condition at $x = x_0$.

We use Equation (54) and its equivalent for the gas component to obtain the steady-state density of every species. Because of the drag force, the velocities are asymptotically equal far away from the shock, allowing the asymptotic right state (+) to be found in terms of the left state (−). Defining the left state as

$$\begin{aligned} \rho_g^- &= \rho_{g0}, \\ \rho_i^- &= \epsilon_i \rho_{g0}, \\ \omega_g^- &= \omega_i^- = 1.0, \end{aligned} \tag{57}$$

the asymptotic right states are

$$\rho_{g/i}^+ = \frac{\rho_{g/i}^- \omega_{g/i}^-}{\omega_{g/i}^+}.$$

$$\omega_g^+ = \omega_i^+ = \left(1 + \sum_{i=1}^{N}\epsilon_i\right)^{-1}\mathcal{M}^{-2}, \tag{58}$$

3.3.2. Numerical Solution

For this test, we solve the cases of one gas combined with one and three dust species, respectively. In Table 3, we summarize the parameters used for each configuration.

We first obtain what we call the exact solution, given by the solution of the initial value problem (integrated numerically) described by Equations (55)–(56), using the left state of the shock as initial condition. We then obtain the numerical solution that results from our implementation.

For the numerical solution, we initialize a discontinuity for both the density and velocity of each fluid. The left and right states are set equal to the asymptotic right steady state as obtained from Equation (58) and given in Table 3. We set the sound speed $c_s = 1$ and the Mach number $\mathcal{M} = 2$, implying $v_s = 2$. The dust-to-gas mass ratio for all dust species is set to $\epsilon = 1$, so the left states are all equal. The numerical domain spans from $x = 0$ to $x = 40$, sampled over 400 evenly spaced grid points, and the initial jump condition occurs at $x = 4$. We use zero gradient boundary conditions.

In Figure 5, we plot the exact (solid lines) and numerical (open circles) solution for both the two- (left panels) and four-fluid (right panels) shock tests. We plot the normalized velocity and density for both the gas and dust fluids in the upper and lower panels, respectively. Different colors correspond to different species. To compare the numerical solution with the exact one, we shifted the exact solution to the shock position. The numerical solution corresponds to a snapshot taken at $t = 500$, a time that is long enough that no significant variation of the numerical solution is observed. The unfilled circles in the main panels are a subsampling (1:6) of the grid points. Inside

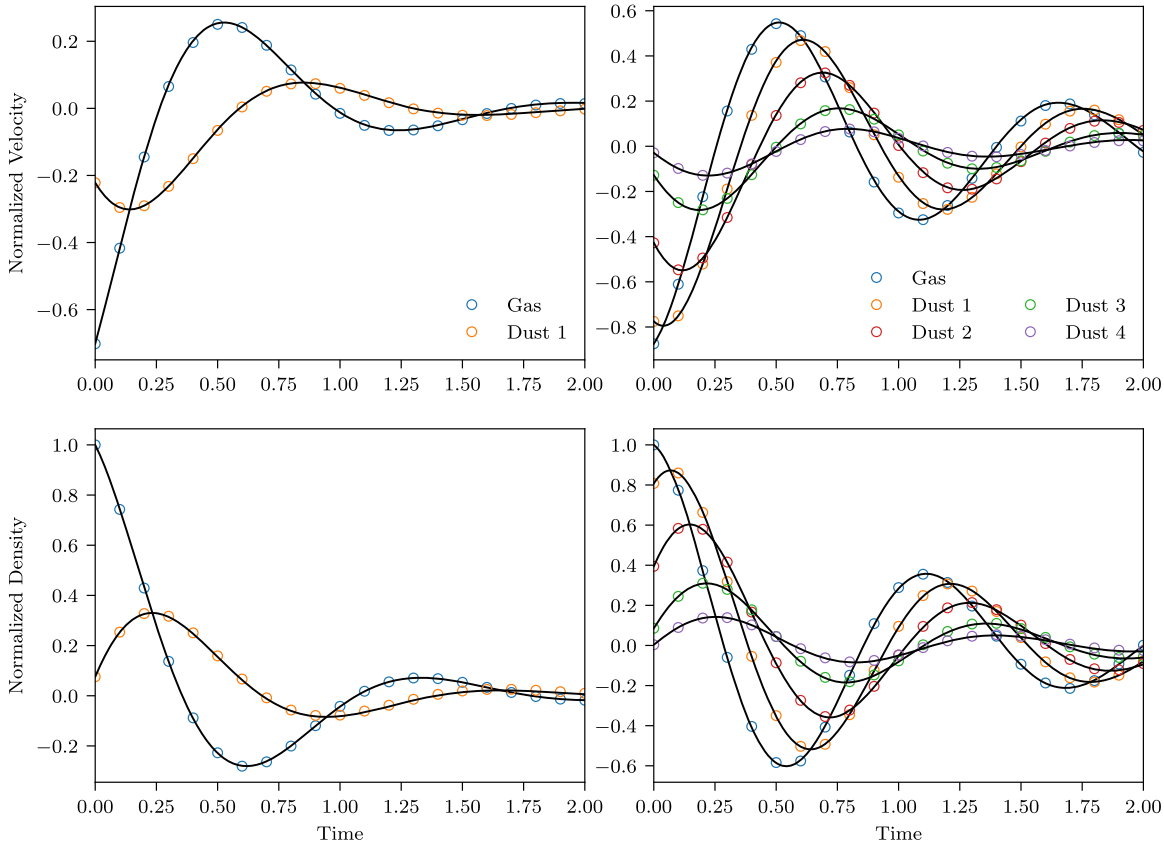

Figure 3. Numerical (open circles) and analytical (solid lines) solutions of the test described in Section 3.2 for the configurations listed in Table 2. We plot the time evolution of the normalized velocity (upper panels) and density (lower panels). The results for one and four dust species are shown in the left and right panels, respectively. The blue circles correspond to the gas, while the other colors correspond to the dust species. All of the solutions were obtained at $x = 0$. The normalized density and velocity are defined as $\delta\hat{\rho}/(A\rho^0)$ and $\delta\hat{v}/(Ac_s)$, respectively, with $A = 10^{-4}$.

each panel, we plot a zoomed-in region containing the discontinuity to show the quality of the numerical solution across the shock in the actual grid.

This test indicates that, as expected, the code resolves a shock within four cells (see Benítez-Llambay & Masset 2016). It furthermore shows that our implementation is able to recover the correct solution across the shock for all the gas and dust species. The agreement between the exact and numerical solutions is excellent, successfully demonstrating the ability of the code to correctly resolve the shock dynamics.

3.4. Steady-state First-order Disk-drift Solutions

In this section, we test the coupling between the collision step and the source and transport steps in our numerical scheme. To accomplish this, we first find the steady-state radial drift solution for an arbitrary number of species to first order in the velocities with respect to an exact background. We then compare this analytical solution with the numerical one. The background is obtained by considering pressure gradients (which are not necessarily small) and ignoring drag forces between species. This solution generalizes that obtained by Nakagawa et al. (1986), who presented a self-consistent first-order solution with respect to a Keplerian background for a disk, composed of gas and one dust species. In their approach, the background flow is obtained as the solution of the vertically integrated disk equations when ignoring pressure and drag forces. This assumption implies that both the radial pressure gradient and the drag force are small perturbations that can be added linearly to the Keplerian velocity. However, the assumption of a small pressure gradient is not strictly necessary to find a background solution.

This generalization provides us with improved steady-state disk models, which allow us to thoroughly test our numerical method.

3.4.1. Generalized Steady-state Drift Solutions

In order to find the background solution for the radial drift problem, we work with the vertically integrated disk equations with an isothermal equation of state, in which the pressure $P = c_s^2\Sigma$, with c_s the sound speed and Σ the surface density. Defining the aspect ratio $h = c_s(r)/v_K$, where v_K is the Keplerian speed and the functions

$$\eta \equiv \frac{h^2}{2}\frac{d\log P}{d\log r}, \qquad \beta \equiv \sqrt{1 + 2\eta(r)}\,, \tag{59}$$

and after ignoring the drag force in the momentum equations, the exact background solution is

$$\boldsymbol{v}_g^0 = \beta(r)\boldsymbol{v}_K, \tag{60}$$

$$\boldsymbol{v}_i^0 = \boldsymbol{v}_K, \tag{61}$$

for $i = 1, \ldots, N$.

When the collision term between species is considered, as an approximation we can assume that the velocity is slightly modified so that it can be written as the background solution, Equations (60)–(61), plus a small deviation, i.e., $\boldsymbol{v} = \boldsymbol{v}^0 + \delta\boldsymbol{v}$.

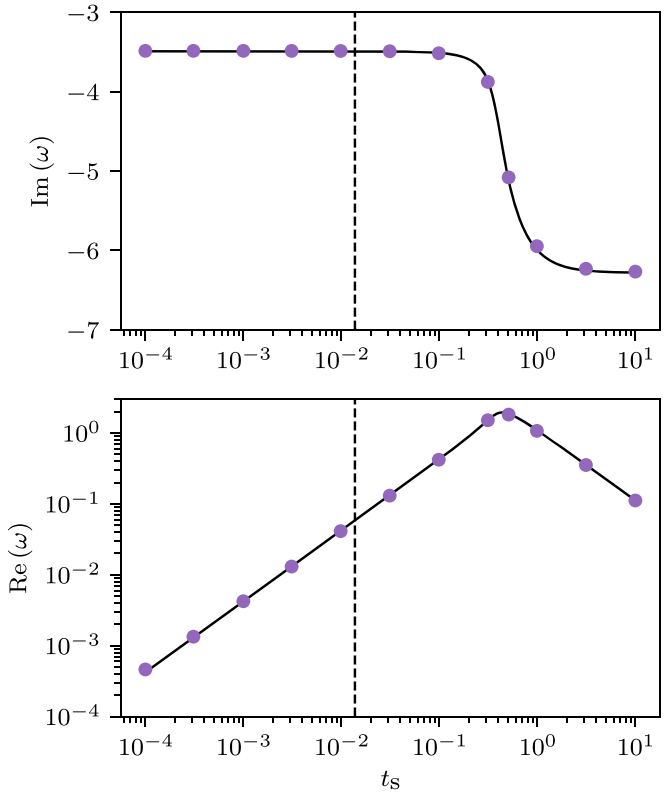

Figure 4. Numerical (circles) and analytical (solid lines) imaginary and real parts of the eigenvalue ω, as a function of the stopping time t_s, obtained for the two-fluid case described in Table 2. The dashed line corresponds to the time step $\Delta t = 1.375 \times 10^{-2}$, which is fixed for all the runs.

Table 3
Parameters for the Dusty Shock Test

Fluids	K_1	K_2	K_3	ρ^-	ρ^+	ω^-	ω^+
2	1.0	⋯	⋯	1.0	8.0	1.0	0.125
4	1.0	3.0	5.0	1.0	16.0	1.0	0.0625

Note. For the two cases, we define $\mathcal{M} = 2$, $c_s = 1$, and $\epsilon = 1$ for every dust species.

Defining the function

$$\xi \equiv \beta\left(\frac{1}{2} + \frac{d\log\beta}{d\log r}\right) \tag{62}$$

and ignoring terms which are second-order in the perturbations, the steady-state axisymmetric Navier–Stokes equations lead to the following set of algebraic equations for the perturbed velocities

$$-2\beta\delta v_{g\varphi} + \sum_{i=1}^{N}\frac{\epsilon_i}{T_{si}}(\delta v_{gr} - \delta v_{ir}) = 0, \tag{63}$$

$$\xi\delta v_{gr} + \sum_{i=1}^{N}\frac{\epsilon_i}{T_{si}}(\delta v_{g\varphi} - \delta v_{i\varphi}) = (1-\beta)v_K\sum_{i=1}^{N}\frac{\epsilon_i}{T_{si}}, \tag{64}$$

$$-2\delta v_{i\varphi} + \frac{1}{T_{si}}(\delta v_{ir} - \delta v_{gr}) = 0, \tag{65}$$

$$\frac{1}{2}\delta v_{ir} + \frac{1}{T_{si}}(\delta v_{i\varphi} - \delta v_{g\varphi}) = \frac{(\beta-1)v_K}{T_{si}}, \tag{66}$$

for $i = 1, ..., N$, with T_s the Stokes number (see Equation (27)). Equations (63)–(66) must be solved coupled with the continuity equations:

$$\partial_r(r\Sigma_g^0\delta v_{gr}) = 0, \tag{67}$$

$$\partial_r(r\Sigma_i^0\delta v_{ir}) = 0. \tag{68}$$

From Equations (65) and (66), we obtain the dust velocities in terms of the gas velocity, which, in combination with Equations (63) and (64), allow us to find the gas velocity perturbations. Defining

$$\mathcal{S}_N \equiv \sum_{i=1}^{N}\frac{\epsilon_i}{1+T_{si}^2}, \qquad \mathcal{Q}_N \equiv \sum_{i=1}^{N}\frac{\epsilon_i T_{si}}{1+T_{si}^2}, \tag{69}$$

the gas velocity perturbations read

$$\delta v_{gr}(r) = -2\beta\mathcal{Q}_N\Psi(\beta-1)v_K, \tag{70}$$

$$\delta v_{g\varphi}(r) = -[(\mathcal{S}_N+2\xi)\mathcal{S}_N + \mathcal{Q}_N^2]\Psi(\beta-1)v_K, \tag{71}$$

with $\Psi \equiv [(\mathcal{S}_N+\beta)(\mathcal{S}_N+2\xi) + \mathcal{Q}_N^2]^{-1}$.

Finally, the expressions for the dust velocity perturbations are

$$\delta v_{ir} = \frac{2T_{si}}{1+T_{si}^2}(\beta-1)v_K + \frac{\delta v_{gr} + 2T_{si}\delta v_{g\varphi}}{1+T_{si}^2}, \tag{72}$$

$$\delta v_{i\varphi} = \frac{1}{1+T_{si}^2}(\beta-1)v_K + \frac{2\delta v_{g\varphi} - T_{si}\delta v_{gr}}{2(1+T_{si}^2)}. \tag{73}$$

The velocities given by Equations (70) and (73) are the solutions only if they satisfy the continuity Equations (67) and (68). For simplicity, in this work, we focus on the particular case of non-flared disks (i.e., $h = h_0$, with h_0 being not necessarily small), where $\beta = \beta_0$ and $\xi = \beta_0/2$. Thus, all of the velocity perturbations scale with the Keplerian speed, v_K, and the background surface-density profiles are power laws with exponent $d\log\Sigma/d\log r = -1/2$.

When considering only one dust species and $h \ll 1$, we can write $\beta \simeq 1+\eta$, and Equations (70)–(73) are the solutions found by Nakagawa et al. (1986). Dipierro et al. (2018) found a similar solution for an arbitrary number of species for a viscous disk assuming a Keplerian background. This solution can be easily improved following our approach.

3.4.2. Numerical Solution

We now use the steady-state solution found in the previous section to test our implementation. For this test, we initialize a large-scale 1D disk using the first-order steady-state solutions, given by Equations (70)–(73). The computational domain spans from $r = 1$ to $r = 100$, evenly spaced in a logarithmic grid over 1024 points. We assume an isothermal equation of state. We set boundary conditions equal to the steady-state solution for all species. The absence of perfect numerical equilibrium at the beginning of the runs produces wave patterns that propagate in the disk and reach the boundaries of the mesh. To remove these spurious waves from the active domain, we use small damping zones close to the boundaries (de Val-Borro et al. 2006). These buffers extend over a region such that $\Delta\Omega = 0.1$ for both the inner and outer buffers (see Benítez-Llambay et al. 2016), and the damping rate is set to one-third of the local Keplerian frequency. We only damp the density and radial velocity to the value given by the initial condition.

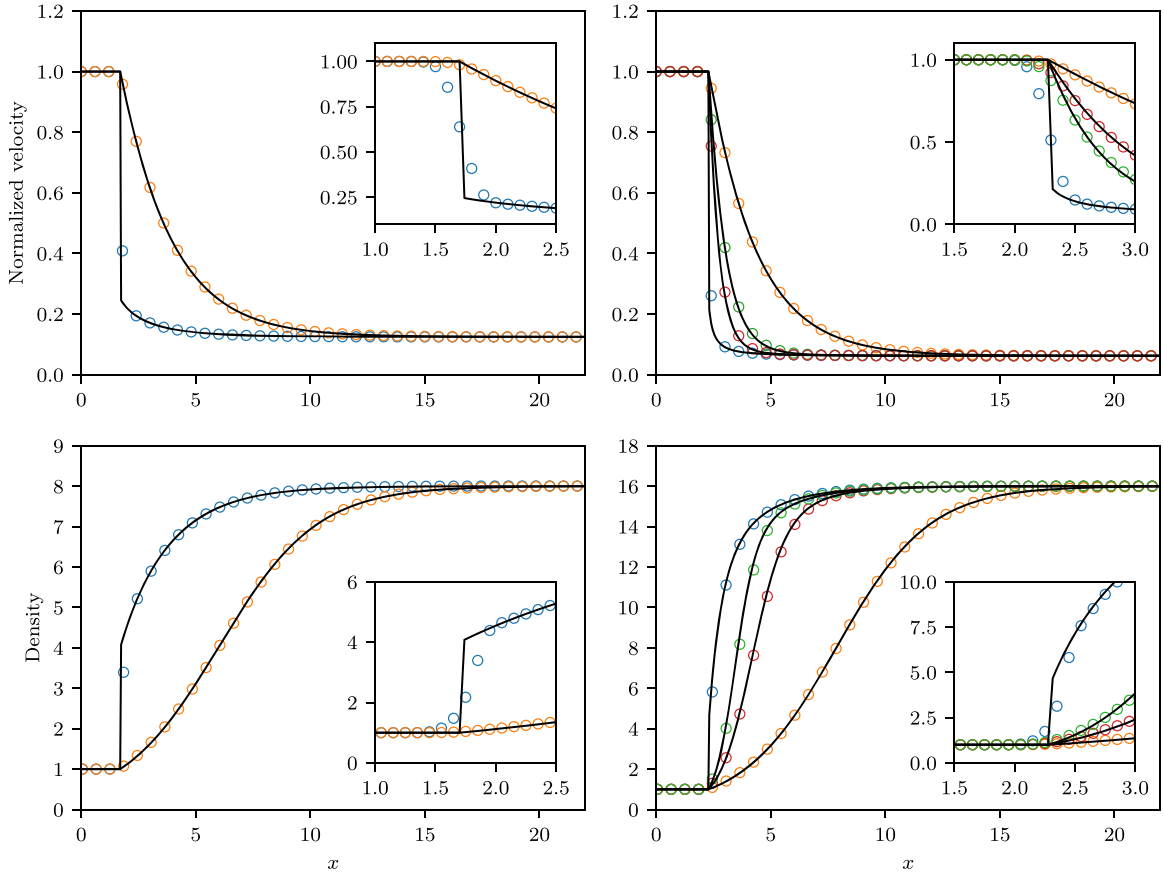

Figure 5. Numerical (open circles) and analytical (solid lines) solutions for the shock test problem, described in Section 3.3, when considering two (left panels) and four (right panels) species. The numerical solution was obtained at time $t = 500$, starting from an initial jump condition. The upper panels show the normalized velocities ω_g, ω_i of the gas (blue) and dust (orange, red, and green) species, respectively. The lower panels show the density of the gas and dust species, sharing the same color code. In the large panels, to allow the quality of the asymptotic behavior far away from the shock to be assessed, the sampling rate for the open circles was reduced to 1:6 of the original data. We additionally plot, inside each panel, a zoomed region within the shocks showing the full sampling, i.e., the unfilled circles correspond to the actual grid points. The code resolves the shock with three to four cells, even when an increasing number of fluids is considered. The overall agreement between the numerical and analytical solutions is excellent.

We consider two cases with two species and two cases with four species, and vary the degree of coupling between the gas and dust species. To test our implementation in more challenging regimes, for each configuration, we furthermore vary the aspect ratio, h, of the disk, adopting the values $h \in [0.05, 0.1, 0.15]$. In order to satisfy the hypothesis when deriving the analytical solution, we work with non-flared disks. In all cases, we numerically integrate the 1D disks until steady state is reached. The initial surface density of the gas component is not relevant for these tests.

In Figure 6, we plot the radial velocity for all cases studied. The results corresponding to different species and different parameters are shown in each column and row, respectively. From top to bottom, in the first two rows, we plot the radial velocity for the two-fluid configurations and, in the last two rows, the radial velocity for the test with four fluids. The analytical solutions, given by Equations (70) and (72), are plotted with solid lines. The different colors represent different species. Furthermore, depending on the adopted aspect ratio, we plot the data set using different symbols. The parameters corresponding to each species are quoted inside of the panels. We observe that the agreement between the analytical and numerical solutions is excellent, and independent of the parameters and the number of species. The tests presented here validate simultaneously the first-order steady-state disk-drift solution and our numerical implementation.

We note an interesting result from the multiple fluid test. In the two-fluid cases, because of momentum conservation, it is impossible to revert the sign of the radial velocity of the dust component, but its magnitude depends on the dust-to-gas mass ratio as well as to the degree of coupling to the gas. However, this is no longer true in the more general case of multiple species. In this case, very well-coupled dust can drift outward with the gas (see, for example, the fourth panel of the third row and the second and third panels of the fourth row). We finally comment that the same level of agreement was observed for the azimuthal velocity, which is not surprising given that the two directions are coupled.

3.4.3. Convergence Test

We additionally performed a convergence test with resolution. This test consists in taking one particular case and measuring the error of the numerical solution when changing the resolution. For this particular case, we defined the error as

$$\mathrm{error}(\Delta r) = \frac{1}{N}\sum_{j=1}^{N}\left\langle \frac{v_{jr}^{\Delta r} - v_{jr}}{v_{jr}} \right\rangle^2, \tag{74}$$

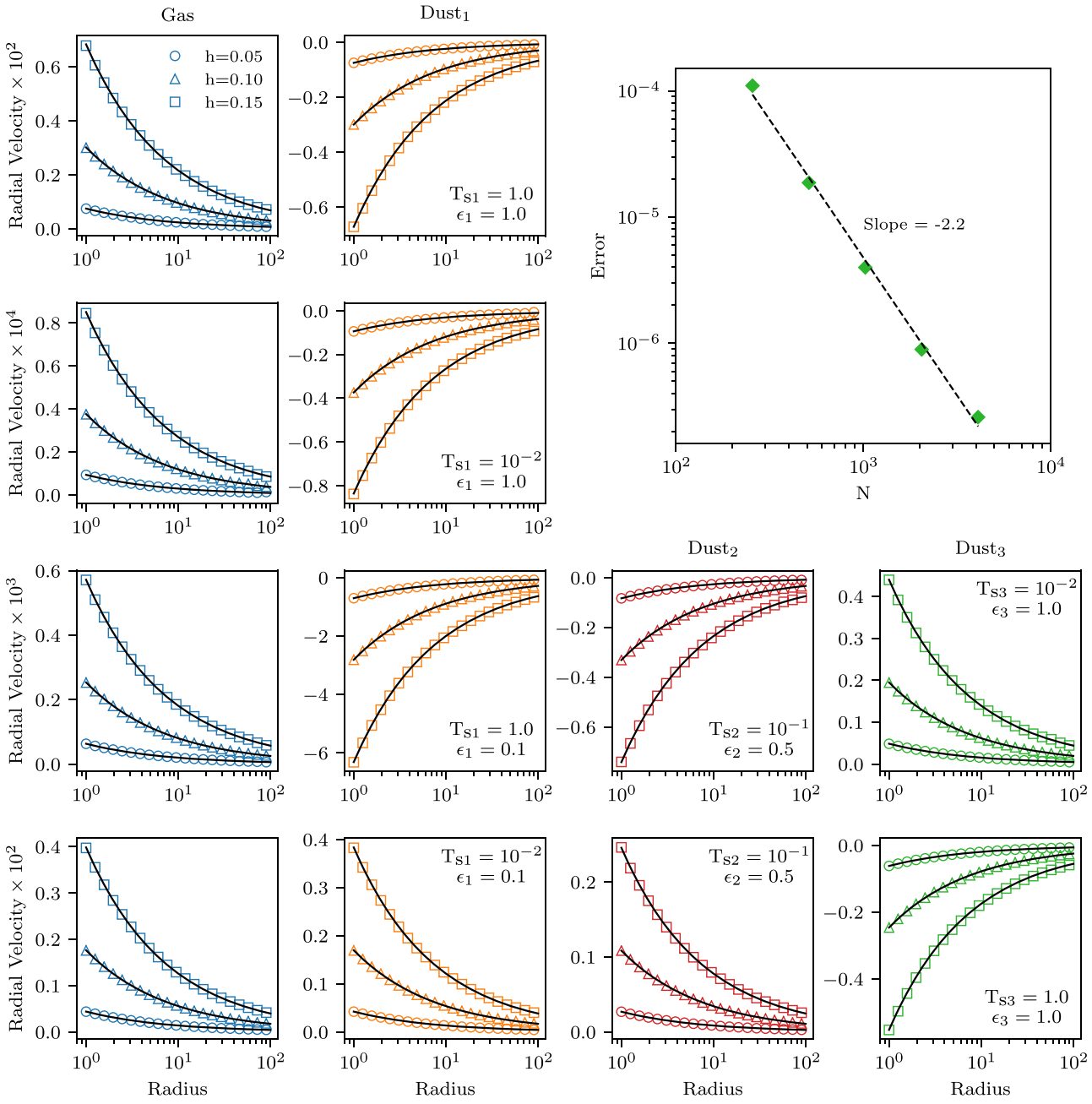

Figure 6. Analytical (solid lines) and numerical (unfilled colored symbols) solutions for the first-order dust radial drift test problem, described in Section 3.4.1. The analytical solutions are given by Equations (70) and (72). In the smaller panels, we plot the radial velocity for all cases studied. Different columns correspond to different species (labeled at the top of each of the uppermost panels) while different rows correspond to runs with different parameters. For each set of parameters, we run the same test with different aspect ratios, h, and plot the resulting radial velocity with different symbols (see the legend in the leftmost upper panel). The parameters of each run are quoted inside of the small panels. In the large panel located on the upper right corner, we additionally plot the result from the convergence test described in Section 3.4.3.

with N the total number of species and $v_{jr}^{\Delta r}$ the solution obtained for different resolutions. We denote the average over the cells with $\langle\rangle$.

For this test, we take the case corresponding to the fourth row of Figure 6. For this particular problem, we find that 256 cells are enough to obtain a converged solution. We then use 256 as the starting number of grid points and go up to 4096, progressively increasing by factors of 2.

We plot the result of this convergence test in the large panel of Figure 6. We successfully recovered a convergence rate close to the expected order of the numerical method. For this test, the time step was allowed to vary according to the CFL condition. Thus, since the errors in space decrease rapidly, the convergence rate is dominated by the first-order error in time.

3.5. Streaming Instability

The aerodynamic coupling between solids and gas in a differentially rotating disk leads to the so-called streaming instability (Youdin & Goodman 2005). Particular modes of this instability have been extensively studied both in linear and nonlinear regimes. This is an excellent problem to test our implementation both in the linear and in the nonlinear regimes.

Due to the complexity of the problem and the degree of coupling between all of the equations and directions, even recovering linear solutions can be a stringent test.

In this paper, we extend previous studies in the linear regime to the case of multiple dust species. In addition, to compare with previous works, we show results in the nonlinear regime considering only one gas and one dust species.

3.5.1. Preliminaries

The growth rate of the streaming instability can be obtained, in its simplest form, by solving the 2.5D linearized axisymmetric shearing-box equations for gas and one dust species. The fluid equations are usually linearized around the steady-state drift solution obtained by Nakagawa et al. (1986). However, in order to study the instability for an arbitrary number of dust species, generalized background solutions are needed. These are similar to the approximated solutions obtained for the a global disk (see Section 3.4.1), but in this case are analytical and exact. We derive and write them explicitly in Section 3.5.2.

In the shearing-box approximation, a self-consistent aerodynamic drag between gas and dust cannot be obtained. However, the instability can still be studied in this formalism by adding an external constant force mimicking the effect of a constant pressure gradient within the box (see, e.g., Bai & Stone 2010).

The equations leading to the streaming instability, when N dust species are considered, are

$$\partial_t \rho_{\rm g} + \nabla \cdot (\rho_{\rm g} \boldsymbol{v}_{\rm g}) = 0, \tag{75}$$

$$\partial_t \rho_j + \nabla \cdot (\rho_j \boldsymbol{v}_j) = 0, \tag{76}$$

$$\partial_t \boldsymbol{v}_{\rm g} + \boldsymbol{v}_{\rm g} \cdot \nabla \boldsymbol{v}_{\rm g} = -\frac{\nabla P}{\rho_{\rm g}} + \chi_0 \Omega_0 \boldsymbol{e}_x + 2q\Omega_0^2 x \boldsymbol{e}_x - 2\boldsymbol{\Omega}_0 \times \boldsymbol{v}_{\rm g} - \Omega_0 \sum_{k=1}^{N} \frac{\epsilon_k \boldsymbol{\Delta}_k}{T_{sk}}, \tag{77}$$

$$\partial_t \boldsymbol{v}_j + \boldsymbol{v}_j \cdot \nabla \boldsymbol{v}_j = 2q\Omega_0^2 x \boldsymbol{e}_x - 2\boldsymbol{\Omega}_0 \times \boldsymbol{v}_j + \Omega_0 \frac{\boldsymbol{\Delta}_j}{T_{sj}}, \tag{78}$$

for $j = 1, \cdots, N$, with q the shear parameter. The term $\chi_0 \Omega_0$ is the constant radial acceleration that mimics the pressure gradient within the box, with χ_0 an arbitrary constant speed. It is usually chosen to reproduce the drift speed of dust in PPDs, i.e., $\chi_0 = 2h_0^2 v_{\rm K0}$, with $h_0 = c_{\rm s0}/v_{\rm K0}$ and $c_{\rm s0}$ the constant sound speed. The unit vector along the radial direction is denoted as $\boldsymbol{e}_x$. The pressure is related to the density as $P = c_{\rm s0}^2 \rho_{\rm g}$. The other terms depend on the dust-to-gas mass ratio $\epsilon_i \equiv \rho_i/\rho_{\rm g}$, the Stokes number T_{si}, and the relative velocity vector between species $\boldsymbol{\Delta}_i = \boldsymbol{v}_{\rm g} - \boldsymbol{v}_i$, where $\boldsymbol{v}_{\rm g}$ and $\boldsymbol{v}_i$ are the gas and dust velocity vectors, respectively.

3.5.2. Steady-state Solution

As discussed above, when setting a constant background density for the gas and all dust species, an exact steady-state solution can be found. This solution is the generalization of that obtained by Nakagawa et al. (1986), and the procedure to find it is similar to that followed when finding the solution for the perturbations in Section 3.4.1. Defining

$$\mathcal{A}_N = \tilde{\kappa}^2 \sum_{i=1}^{N} \frac{\epsilon_i T_{si}}{1 + \tilde{\kappa}^2 T_{si}^2}, \tag{79}$$

$$\mathcal{B}_N = 1 + \sum_{i=1}^{N} \frac{\epsilon_i}{1 + \tilde{\kappa}^2 T_{si}^2}, \tag{80}$$

the steady-state solution of Equations (75)–(78) is

$$v_{{\rm g}x}^0 = \mathcal{A}_N \chi_0 \psi, \tag{81}$$

$$v_{{\rm g}y}^0 = -q\Omega_0 x - \frac{\tilde{\kappa}^2}{2} \mathcal{B}_N \chi_0 \psi, \tag{82}$$

with $\psi = (\mathcal{A}_N^2 + \tilde{\kappa}^2 \mathcal{B}_N^2)^{-1}$ and $\tilde{\kappa}^2 = \kappa^2 \Omega_0^{-2}$, where $\kappa^2 = 2(2-q)\Omega_0^2$ is the square of the epicyclic frequency.

For the ith dust species, its velocity can be written in terms of the velocity of the gas as

$$v_{ix}^0 = \frac{v_{{\rm g}x}^0 + 2T_{si}(v_{{\rm g}y}^0 + q\Omega_0 x)}{1 + \tilde{\kappa}^2 T_{si}^2}, \tag{83}$$

$$v_{iy}^0 = -q\Omega_0 x + \frac{(v_{{\rm g}y}^0 + q\Omega_0 x) - (2-q) T_{si} v_{{\rm g}x}^0}{1 + \tilde{\kappa}^2 T_{si}^2}. \tag{84}$$

The vertical velocities are $v_{{\rm g}z}^0 = v_{iz}^0 = 0$ and the densities are constant for all species. We note that, for the case $q = 3/2$ (i.e., Keplerian shear), Equations (81)–(84) are, as expected, equivalent to the expansion of Equations (70)–(73) for $h_0 \ll 1$.

3.5.3. Linear Regime—Eigenvalues and Eigenvectors

Assuming solutions of the form $\delta\rho = \rho^0 + \delta\rho$, $\boldsymbol{v} = \boldsymbol{v}^0 + \delta\boldsymbol{v}$, and after ignoring quadratic terms in the perturbations, Equations (75)–(78) become a set of linear partial differential equations for the perturbations δ. Without loss of generality, we assume perturbations of the form $\delta f(x, z, t) = \delta\hat{f}\, e^{i(k_x x + k_z z) - \omega t}$, from which Equations (75)–(78) transform into a set of linear algebraic equations of the form

$$\boldsymbol{A}\boldsymbol{u} = \tilde{\omega}\boldsymbol{u}, \tag{85}$$

with $\boldsymbol{u}$ the column vector whose elements are the perturbation amplitudes and $\tilde{\omega} = \omega/\Omega_0$ the normalized eigenvalues. The problem then reduces to finding the normalized eigenvalues and eigenvectors of the $N \times N$ matrix $\boldsymbol{A}$. We write the explicit expression of this linear system in Appendix E.

A general expression for the dispersion relation and its eigenvectors can be easily obtained and written in closed form (similarly to what was done in Section 3.2). However, due to the complexity of these expressions, we avoid writing them here. Instead, when solving the eigenvalue problem, we simply write the matrix $\boldsymbol{A}$ and find its eigenvalues and eigenvectors numerically.

In Table 4, we present the parameters, the eigenvalues, and the eigenvectors for the three different cases studied in this paper, called LinA, LinB, and Lin3. The first two cases correspond to one gas and one dust species and have already been studied (e.g., Youdin & Johansen 2007; Balsara et al. 2009; Bai & Stone 2010). The third one contains one gas and two dust species.

We report a small difference with respect to the eigenvalues obtained by Youdin & Johansen (2007). We tracked down the difference to two terms in the linearized equations (see

Table 4
Eigenvalues, Eigenvectors, and Parameters for Runs LinA, LinB and Lin3

	LinA	LinB	Lin3
Parameters			
K	30	6	50
T_{s1}	0.1	0.1	0.0425
ϵ_1	3.0	0.2	1.0
T_{s2}	⋯	⋯	0.1
ϵ_2	⋯	⋯	0.5
Eigenvalue			
ω/Ω_0	$-0.4190091323 + 0.3480181522i$	$-0.0154862262 - 0.4998787515i$	$-0.3027262829 + 0.3242790653i$
Eigenvector			
$\delta\tilde{\rho}_g$	$+0.0000074637 + 0.0000070677i$	$-0.0000337227 - 0.0003456248i$	$+0.0000061052 + 0.0000080743i$
$\delta\tilde{v}_{gx}$	$-0.0563787907 + 0.0120535455i$	$-0.0870451125 - 1.3851731095i$	$-0.1587288108 + 0.0213251096i$
$\delta\tilde{v}_{gy}$	$+0.0445570113 + 0.0197224299i$	$+1.3839936168 - 0.0937424679i$	$+0.1327989476 + 0.0674232641i$
$\delta\tilde{v}_{gz}$	$+0.0563784989 - 0.0120536242i$	$+0.0870497444 + 1.3852113520i$	$+0.1587286212 - 0.0213252588i$
$\delta\tilde{v}_{1x}$	$-0.0466198076 + 0.0124333223i$	$+0.2314730923 - 1.3715260043i$	$-0.1461274403 + 0.0234873672i$
$\delta\tilde{v}_{1y}$	$+0.0435211557 + 0.0213517453i$	$+1.3696536978 + 0.0196879160i$	$+0.1325843682 + 0.0691301709i$
$\delta\tilde{v}_{1z}$	$+0.0546507401 - 0.0077776652i$	$+0.0416164539 + 1.3844311928i$	$+0.1571142133 - 0.0174328415i$
$\delta\tilde{\rho}_2$	⋯	⋯	$+0.1522281314 + 0.1836379253i$
$\delta\tilde{v}_{2x}$	⋯	⋯	$-0.1335593453 + 0.0025396632i$
$\delta\tilde{v}_{2y}$	⋯	⋯	$+0.1092222067 + 0.0952973332i$
$\delta\tilde{v}_{2z}$	⋯	⋯	$+0.1485545469 + 0.0200753935i$

Note. The dimensionless velocity amplitudes and wavenumbers are defined as $\delta\tilde{v} = \delta v/(h_0^2 v_{K0})$ and $K = k h_0^2 v_{K0}/\Omega_0$, respectively (see Appendix E). The dust density perturbation $\delta\tilde{\rho}_1 = 1$ for all the runs.

Appendix E):

$$-\delta\tilde{\rho}_g \sum_{k=1}^{N} \frac{\epsilon_k^0 \Delta_{kx}^0}{T_{sk}}, \quad \text{and} \quad -\delta\tilde{\rho}_g \sum_{k=1}^{N} \frac{\epsilon_k^0 \Delta_{ky}^0}{T_{sk}}. \tag{86}$$

Ignoring these terms modifies the fourth digit of the eigenvalues and allows us to recover the values reported by Youdin & Johansen (2007).

3.5.4. Linear Regime—Numerical Solution

To test our implementation, we solve the fully nonlinear set of equations in the shearing-box approximation. We then compare the results with those obtained from the linear solution described in the previous section.

To numerically recover the solutions, we set $h_0 = 0.05$ and $v_{K0} = 1$, and add the constant external force χ_0 to the gas component along the x direction. The shear parameter q is set to $3/2$. We only consider wavenumbers $k_x = k_z = k$, so we employ a square axisymmetric shearing box with $x, y \in [-L/2, L/2]$ and $L = 2\pi/k$. The grid is evenly spaced over 256 cells in each direction. We set periodic and shear-periodic boundary conditions in the z and x directions, respectively. The initial condition is given by the steady-state background solution, Equations (81)–(84), and we set the background densities to $\rho_i^0 = \epsilon_i \rho_g^0$, with $\rho_g^0 = 1.0$.

Because of truncation errors, the numerical equilibrium does not match, to machine precision, that given by Equations (81)–(84), but it is very close. However, after initializing each run, the system quickly relaxes toward an exact numerical equilibrium. Thus, to improve our measurements, we wait for a time $t_0 = 1.2\Omega_0^{-1}$ until numerical equilibrium is obtained, and then excite the unstable mode. We note that to speed up the calculations, the relaxation step can be done in a 1D grid. We fix the CFL factor to 0.3 for all runs.

The linear mode is excited by adding to the steady-state background f the small perturbation δf, defined as

$$\delta f = A[\mathrm{Re}\,(\delta\hat{f})\cos(k_x x + k_z z) - \mathrm{Im}\,(\delta\hat{f})\sin(k_x x + k_z z)], \tag{87}$$

where $\delta\hat{f}$ is the complex amplitude of the corresponding component of the unstable eigenvector (see Table 4) and A is a small amplitude that ensures linearity. Its value is set to $A = 10^{-5}$.

In Figure 7, we plot the time evolution of the normalized density perturbations for each of the three different cases, measured from time t_0 at the location $x = z = -L/2$ (this is an arbitrary choice). The normalization is such that the density perturbation is between zero and one for the time interval considered. In each panel we plot, with unfilled circles, the values obtained numerically with our implementation, while the solid lines are the analytical ones. The color represents the different species, blue being the gas, and orange and red the dust species. The first two rows of Figure 7 correspond to the tests LinA and LinB, respectively. The third one corresponds to the three-species Lin3 test. In all of the runs, the agreement between the analytical and numerical solutions is excellent. We additionally comment that the same level of agreement is observed for the velocities of the gas and dust species.

In Table 5, we present the result of the measured growth rates for the tests LinA, LinB and Lin3, for different resolutions. The growth rate for each mode was obtained first by fitting each component of the eigenvector and then averaging the results of the fits. For the tests LinA and Lin3, the instability can be recovered with eight cells. However, for the mode linB, at least 16 cells are required to obtain an

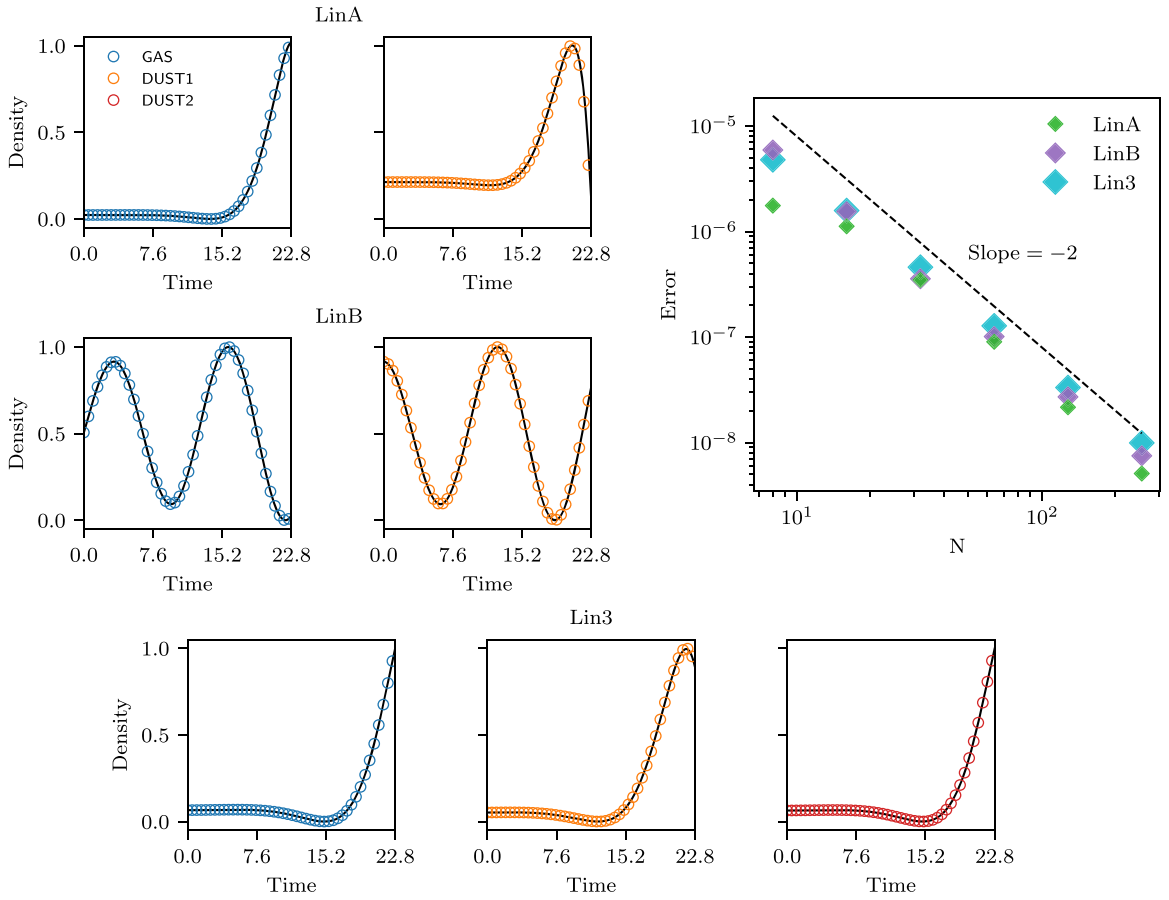

Figure 7. Analytical (solid lines) and numerical (open circles) solutions of the linear streaming instability, described in Section 3.5.4, for the runs LinA (top), LinB (center), and Lin3 (bottom), obtained with 128^2 grid points. From left to right, we plot the gas and dust densities. We additionally plot the result of the convergence test, described in Section 3.5.5. The agreement between the analytical and numerical solutions is excellent. The slope recovered from the convergence test is consistent with the expected convergence rate for all cases, showing small deviations for very low resolutions.

unstable behavior. The errors correspond to the standard deviation of the average.

This test allows us to confidently conclude that our implementation is correct and very robust. In the next section, we additionally study the convergence rate for these test problems.

3.5.5. Linear Regime—Convergence Test

To test the convergence rate of these test problems, we perform a series of runs decreasing the resolutions by factors of 2, starting with 256^2 cells down to 8^2 cells.

We measure the convergence rate for the three configurations described in the previous section by computing the error, defined as

$$\text{error} = \left(\sum_{i=1}^{m} \langle (\delta f_i^{\Delta}(t) - \delta f_i(t))^2 \rangle \right)^{1/2}, \tag{88}$$

where m is the number of components of the eigenvector, δf^{Δ} the numerical solution, δf_i the analytical one, and $\langle\ \rangle$ the time average between $t = t_0$ and $t = 7\Omega_0^{-1}$.

The rightmost large panel of Figure 7 shows the result of the convergence test for the three different cases. We additionally plot (dashed line) the expected second-order accuracy slope. The lowest resolution cases slightly depart from it. However, an excellent convergence rate is observed for $N > 32^2$ grid points. The convergence properties for all of the modes analyzed demonstrate the validity of our implementation. It is remarkable that, even with low resolution, our implementation is able to recover the linear growth rate with an acceptable level of accuracy.

We report that we have observed the mode LinB to be prone to develop noise at cell level, which, eventually, contaminates the computational domain. By disabling the drag term, we have concluded that this noise is something entirely related to the gas component. This issue was significantly reduced by enabling a predictor using a half transport step before the source step, allowing us to recover excellent second-order-accurate linear solutions (see Section 2.4).

3.5.6. Nonlinear Regime

To study the nonlinear regime of the streaming instability, we consider the runs AB and BA described by Johansen & Youdin (2007) and Bai & Stone (2010). We focus our attention on the convergence with resolution, the cumulative dust density distribution, and the time evolution of the maximum density. These tests give us, in particular, the opportunity to assess whether the Eulerian approach for the dust species is able to reproduce features similar to those obtained by Bai & Stone (2010) using Lagrangian particles.

For each test, we set a square shearing box of size $L = lh_0H_0$, with $h_0 = 0.05$, $H_0 = h_0R_0$, and the fiducial radius $R_0 = 1$. The shear parameter q is, as above, $3/2$ (i.e., Keplerian

Table 5
Measured Growth Rates for Different Numbers of Cells for Runs LinA, LinB, and Lin3

N	LinA	LinB	Lin3
8	$-0.325 \pm 3.3 \times 10^{-2}$	$0.0301 \pm 1.2 \times 10^{-3}$	$-0.222 \pm 8.5 \times 10^{-2}$
16	$-0.3961 \pm 1.7 \times 10^{-3}$	$-0.00821 \pm 2.9 \times 10^{-4}$	$-0.271 \pm 4.9 \times 10^{-2}$
32	$-0.41311 \pm 5.2 \times 10^{-4}$	$-0.014468 \pm 7.3 \times 10^{-5}$	$-0.291 \pm 1.3 \times 10^{-2}$
64	$-0.41762 \pm 1.5 \times 10^{-4}$	$-0.015349 \pm 2.2 \times 10^{-5}$	$-0.3000 \pm 2.4 \times 10^{-3}$
128	$-0.418583 \pm 8.0 \times 10^{-5}$	$-0.0154688 \pm 6.5 \times 10^{-6}$	$-0.30248 \pm 1.4 \times 10^{-4}$
256	$-0.418900 \pm 5.4 \times 10^{-5}$	$-0.0154839 \pm 2.0 \times 10^{-6}$	$-0.302672 \pm 5.1 \times 10^{-5}$

Note. The values correspond to the average of the growth rates obtained by fitting the time evolution of each component of the eigenvector. The errors correspond to the standard deviation of this average.

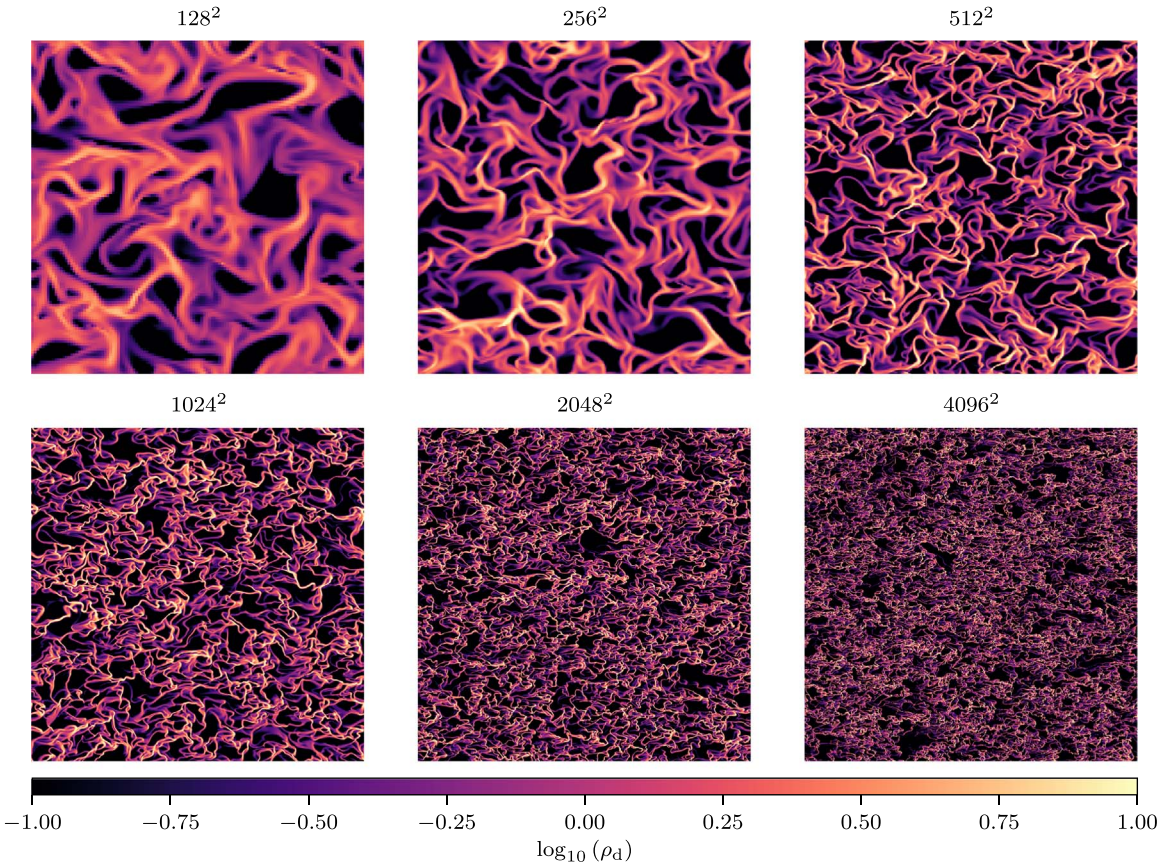

Figure 8. Dust density maps for the test AB. Each panel is labeled by the total number of cells of the box. This mode is dominated by overdense filaments and voids. The larger the resolution, the smaller and denser the filaments become. Convergence with resolution is far from being observed for the resolutions studied. The panels corresponding to 256^2 and 1024^2 cells can be compared with Figure 5 of Bai & Stone (2010), where a good qualitative agreement is observed.

rotation). For the test AB (BA), we set the dust-to-gas mass ratio $\epsilon_1 = 1$ ($\epsilon_1 = 0.2$), the Stokes number $T_{s1} = 0.1$ ($T_{s1} = 1.0$), and the parameter $l = 2$ ($l = 40$). The total integration time is set to $40\Omega_0^{-1}$ ($800\Omega_0^{-1}$), which allows the saturated turbulent state to be reached (Bai & Stone 2010). We seed the instability with white noise in the three velocity components of the two species, with an amplitude $A = 10^{-2} h_0 v_{K0}$.

To test convergence with resolution, for a fixed box size, we vary the number of grid cells by a factor of 4. For the test BA, we set the nominal box with 64^2 cells—a resolution of roughly $32/H_0$—and obtain results when varying the number of cells up to 2048^2—a resolution of $1024/H_0$. For the test AB, because a box with 64^2 cells does not allow the instability to growth, we start with 128^2 cells—a resolution of $1280/H_0$—and increase it up to 4096^2 cells—a resolution of 40, $960/H_0$. We note that, when using 64^2 cells for run AB, Bai & Stone (2010) were able to recover an unstable evolution, which is probably due to the higher order of the Athena code. For run AB and the lowest resolution (128^2 grid cells), we report a saturation time $\simeq 12\Omega_0^{-1}$, a value highly dependent on resolution. On the other hand, for the case BA and the lowest resolution (64^2 grid cells), it saturates after $\simeq 150\Omega_0^{-1}$. This value is not very dependent on resolution.

In Figures 8 and 9, we show snapshots of the dust density when the instability is saturated, at times $20\Omega_0^{-1}$ and $400\Omega_0^{-1}$, for the runs AB and BA, respectively. Figure 8 shows that, for the test AB, smaller and denser structures develop when the resolution increases, where no sign of convergence with resolution is observed. This effect, while still present, is not as strong for the low-resolution runs in the test BA (Figure 9). Naively, this can be understood by analyzing the dispersion relation of the instability (see, e.g., Youdin & Johansen 2007).

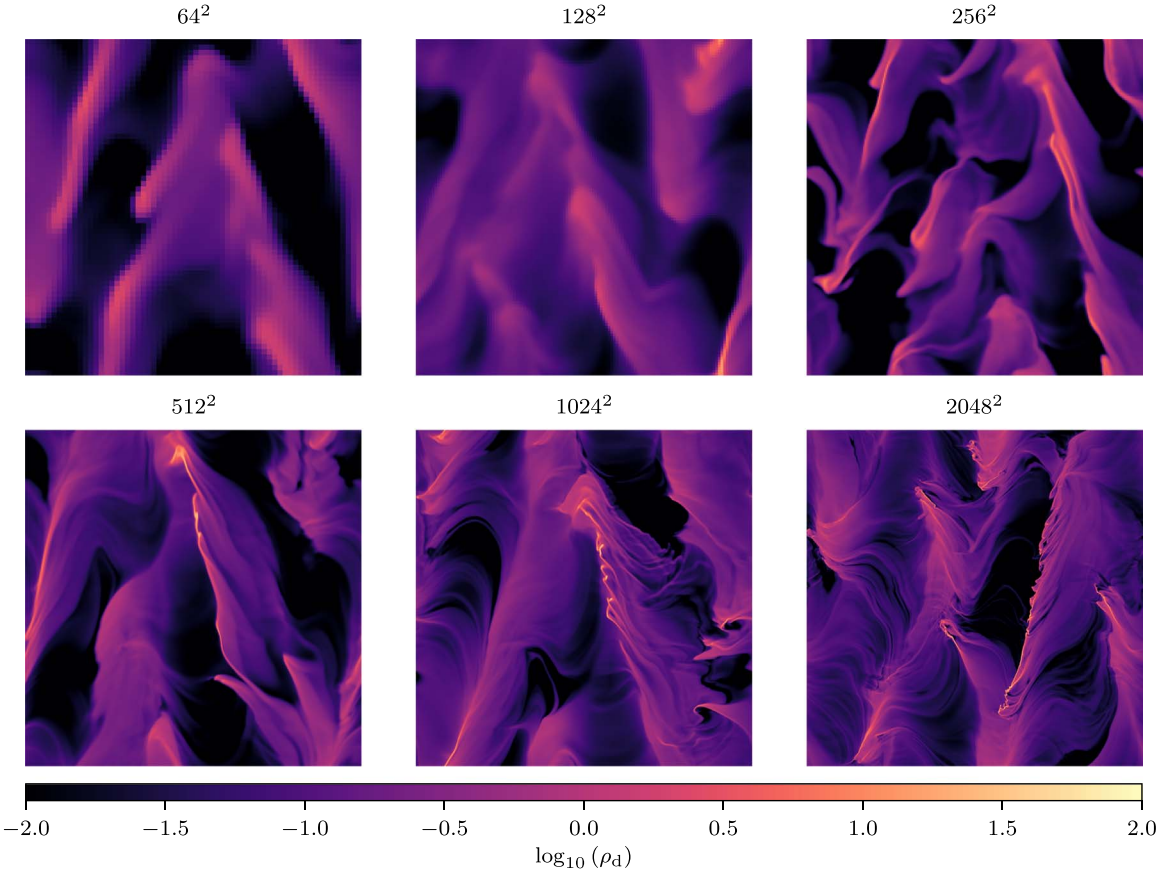

Figure 9. Dust density maps for the test BA. Each panel is labeled by the total number of cells of the box. While the number of details increases with the number of cells, convergence with resolution is observed for number of cells $>512^2$. The panels corresponding to 256^2 and 1024^2 cells can be compared with Figure 5 of Bai & Stone (2010), where a good qualitative agreement is observed.

In the absence of any dissipative process, such as viscosity or diffusion, the smaller scales ($k_z \to \infty$) grow at a rate given by the maximum growth rate. Thus, density concentrations are prone to grow in very localized regions, a trend that can be clearly recognized in Figure 8 for the case AB. We refer to this as a naive explanation because it is not clear that the same occurs for the case BA, even when considering that the dispersion relation is not very different from that obtained for the case AB. Further studies are necessary to understand the real source of the discrepancy in the convergence properties between these two cases.

The panels that correspond to 256^2 and 1024^2 cells can be compared with those presented in Figure 5 of Bai & Stone (2010). The level of qualitative agreement between the dust density obtained using a particle approach (Bai & Stone 2010) and our fluid approach is remarkable. We note that, in the nonlinear turbulent regime, the instability could, in principle, be dominated by crossing trajectories, thus invalidating our approach. However, the overall agreement obtained from this qualitative comparison suggests that the dynamics of the instability, in the nonlinear regime, could be treated using a fluid approach.

To better quantify the convergence properties for both the AB and BA tests, following Youdin & Johansen (2007) and Bai & Stone (2010), we study the cumulative dust density distribution. We calculate it by following two different procedures, one by the counting number of cells with density above some threshold value, $\rho_{\rm threshold}$, and another one by adding up the density of cells with density above $\rho_{\rm threshold}$. The latter is similar to counting the (effective) number of particles, as done by Youdin & Johansen (2007) and Bai & Stone (2010). We split the dust density in 300 logarithmic bins, between $\log_{10}(\rho_a \epsilon)$ and $\log_{10}(\rho_b \epsilon)$, where $\rho_b = 10^2$ for the case AB, while $\rho_b = 2 \times 10^3$ for BA, and $\rho_a = 10^{-1}$ in both cases. To obtain a representative cumulative function of the saturated regime, we compute it for different times, between $t = 30\Omega_0^{-1}$ and $t = 600\Omega_0^{-1}$ for the cases AB and BA, respectively, until the final integration time, and we finally average them. We also compute the standard deviation, which provides valuable information about the fluctuations of the density in the saturated phase.

In Figure 10, we plot the time-averaged cumulative distributions for the dust density, corresponding to the cases AB (upper panels) and BA (lower panels). In each panel, and with different colors, we plot the cumulative function corresponding to the data shown in the panels of Figures 8 and 9. Shaded regions show the standard deviation. The left and right panels show the results obtained by counting the number of cells and by summing the density of the cells, respectively. In the left panels, the distributions are normalized such that they integrate to one. To compare with Bai & Stone (2010), the curves in the right panels are normalized such that the probability of the minimum density bin is one.

For both cases, AB and BA, the dispersion is very small and does not depend on the method used to calculate the cumulative distribution. In particular, for run BA, a strong degree of convergence, down to probabilities of the order

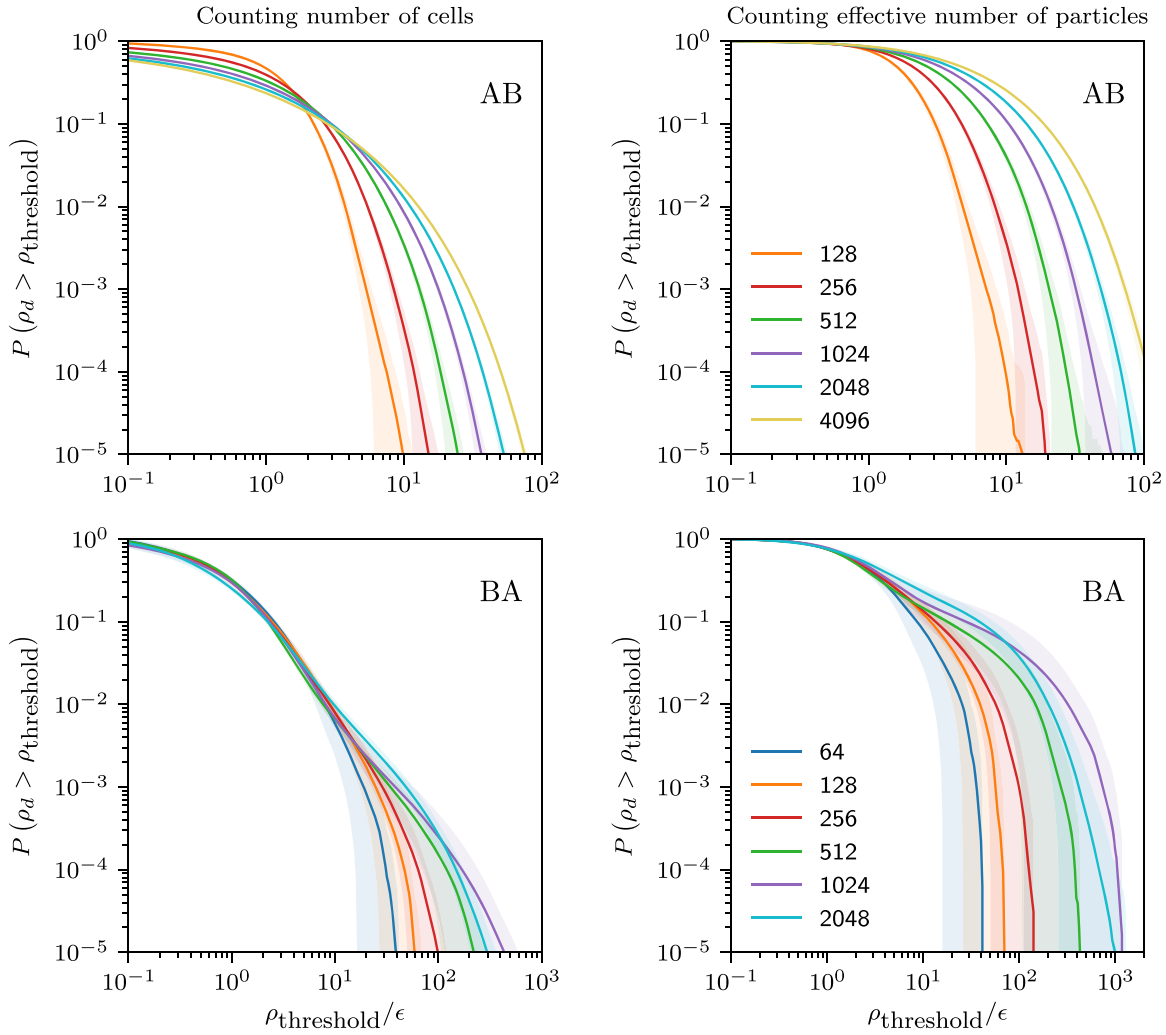

Figure 10. Cumulative dust density distributions for the models AB (top) and BA (bottom). Solid lines correspond to the time-averaged cumulatives. Shaded regions correspond to the standard deviation. The different colors represent each of the cases shown in Figures 8 and 9. The left and right panels show the distributions obtained by counting cells and density, respectively. The distributions are normalized such that they integrate to one (left panels) or the probability of the lowest density threshold is equal to one (right panels). The upper panel shows that, for the mode AB, the maximum density increases linearly with the resolution, a clear evidence of lack of convergence. Contrary to this case, the bottom panel shows that, for a number of cells $>512^2$, the mode BA converges for all the density values. These results are independent of the statistical method used to compute the distributions. The right panels can be directly compared with Figure 6 of Bai & Stone (2010).

$P(\rho_{\rm d} > \rho_{\rm threshold}) \sim 10^{-3}$, is observed for all resolutions. We report that, for $P = 10^{-5}$, the probabilities obtained correspond to values of $\rho_{\rm threshold}/\epsilon$ that are roughly one order of magnitude below the values presented by Bai & Stone (2010) when counting the number of cells. However, counting the (effective) number of particles, by adding up densities, removes this discrepancy. Contrary to what is observed for the case AB, the mode BA seems converged for number of cells larger than 512^2.

The method used to calculate the cumulative distributions does not modify the degree of convergence found for each run, AB and BA. However, the shape of the distributions is method-dependent. When counting cells, lower densities contribute more significantly in shaping the cumulative distribution, while when counting the (effective) number of particles, denser regions contribute more. While the maximum-density values differ from those obtained by Bai & Stone (2010) for run AB, the overall shape of the distributions agrees better when adding up densities.

Run AB shows a direct correlation between the saturation timescale and the resolution, i.e., the higher the resolution, the faster the instability saturates. Furthermore, we find the maximum density to be proportional to the number of cells, a clear evidence of lack of convergence. The previous analysis is supported by Figure 11, where we plot the maximum dust density as a function of time for each case and resolution. As described above, we show again that run BA is much better behaved in terms of convergence. While the maximum density also increases with resolution for the low-resolution cases, it converges when using more than 512^2 cells.

The differences found when comparing our results with those obtained using Lagrangian particles, in particular the lack of convergence for run AB, warrant a detailed comparison between these two approaches.

4. Summary and Perspectives

In this paper, we have presented a reliable numerical method developed to solve the momentum transfer between multiple

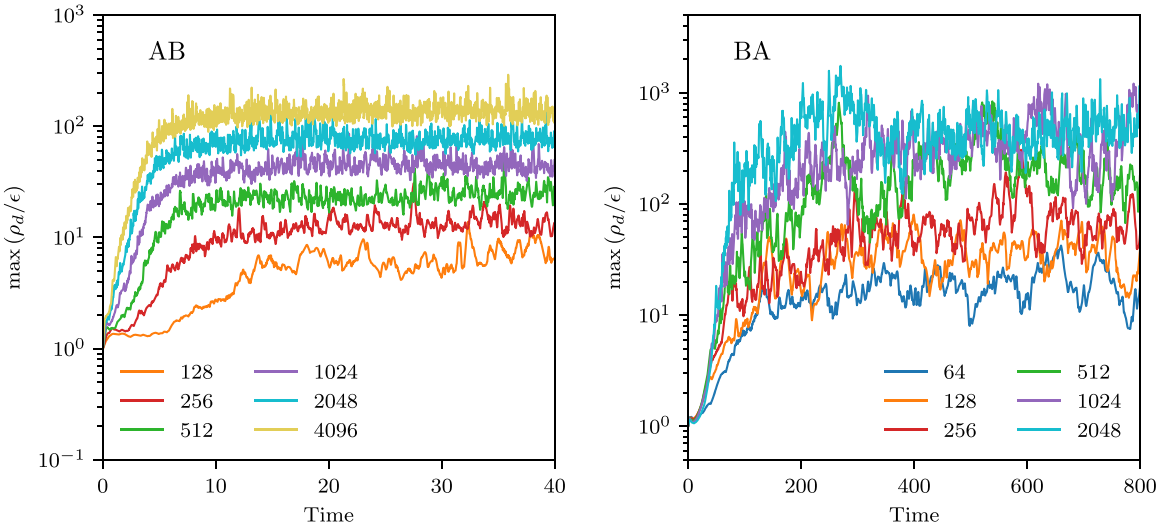

Figure 11. Maximum dust density over time for the modes AB (left panel) and BA (right panel). As shown in Figure 10, the maximum density for case AB increases linearly with resolution. The left panel also shows that the time for saturation is directly correlated with the resolution. In contrast to this case, the mode BA presents much better convergence properties with resolution. The right panel shows that, for low resolution, the initial growth rate directly correlates with resolution. However, for number of cells $>512^2$, convergence in the growth rate is observed. The same degree of convergence is observed for the maximum dust density over the time interval considered, where both the maximum and fluctuations are comparable.

species. We have focused on systems composed of gas and several dust species in the linear drag regime, which has a broad spectrum of applicability in studies of PPDs. Nevertheless, we have also shown in Appendix C, by means of a simple example, how this method could be extended to the nonlinear drag regime.

The core of our implementation is the correct treatment of the coupling term between different species. This is solved using a first-order fully implicit method and connected to the fluid solvers via the operator-splitting approximation. After analyzing different test problems of varying complexity, we have shown that the code conserves its second-order accuracy in space.

The implicit scheme was designed to conserve momentum to machine precision, a quantity that must be conserved during collisions between pairs of species. This property is fundamental to correctly describe the physical evolution of a system of multiple species and makes the solver extremely robust. In addition, we have shown that the implicit scheme is asymptotically and unconditionally stable, with the correct asymptotic limits. Furthermore, this property is independent of the number of species.

Because the value of the Stokes number is not directly involved when studying the properties of the implicit scheme, we stress that the algorithm works well independently of the Stokes number, as was confirmed by our test suite.

Before using this implementation to study a particular physical problem, it is necessary to assess for which Stokes numbers the fluid approximation is expected to produce a good description of the dynamics of the problem. Generally, if the dynamics of the problem is not dominated by crossing trajectories—which are transformed into shocks by the fluid approach—the fluid approach should remain as a good approximation.

A qualitative comparison between Bai & Stone (2010) and this work has shown that the agreement between the particles and the pressureless fluid approximation for dust is very good, while we were not able to find convergence for run AB. Further studies are still needed in order to assess the level of agreement between both approximations.

In this paper, we did not take into account the thermal evolution of the species and the possibility of mass transfer between them. These two ingredients are very important in order to study the self-consistent dust evolution in PPDs. In particular, to properly account for the thermodynamics of the system, models for frictional heating, heat conduction, and radiation should be considered for the gas and dust species.

This implementation has already been successfully used to study problems in the context of PPD dynamics. These are related to planet–disk interactions in dusty disks (Benítez-Llambay & Pessah 2018), dust filtration by giant planets (Weber et al. 2018), and dust accumulation in magnetized PPDs when non-ideal MHD effects are taken into account (Krapp et al. 2018). The robustness of the implicit scheme presented in this work and its versatility for adding an arbitrary number of species in a systematic way, open new possibilities for studying dust dynamics self-consistently in PPDs.

These capabilities are critical in order to investigate a wide range of phenomena in dusty PPDs, including dust growth, dust and planetesimal dynamics, and ultimately, how planets form.

We thank Frédéric Masset for inspiring discussions that motivated this project. We thank Philipp Weber for his valuable contribution based on an early version of our numerical implementation. His input was key to define the flowchart presented in this work. We thank Richard Booth for his demonstration of the importance of the order of the operator splitting when computing the implicit update, discussed in Section 2.4. We thank Andrew Youdin for suggesting to us adding up densities when computing cumulative density distributions in order to ease the comparison between the fluid approach and Lagrangian particles. This project has received funding from the European Union's Horizon 2020 research and innovation programme under grant agreement No. 748544 (P. B.L.). The research leading to these results has received funding from the European Research Council under the

European Union's Horizon 2020 research and innovation programme (grant agreement No. 638596; L.K.). M.E.P. gratefully acknowledges support from the Independent Research Fund Denmark (DFF) via grant No. DFF 8021-00400B. Computations were performed on the `astro_gpu` and `astro_long` partitions of the Steno cluster at the HPC center of the University of Copenhagen.

Software: IPython (Pérez & Granger 2007), NumPy (van der Walt et al. 2011), Matplotlib (Hunter 2007).

Appendix A
Source Terms in the Continuity Equation

Important physical processes can be modeled by means of source terms in the continuity equation. Some examples are dust fragmentation/growth, dust diffusion, and chemical reactions, among others (see, e.g., Weber et al. 2018 for an example on dust diffusion). The continuity equation with a source term (possibly depending on other species) is

$$\frac{\partial \rho_i}{\partial t} + \nabla \cdot (\rho_i \boldsymbol{v}_i) = S_i. \tag{89}$$

It is important to note that the source terms in the continuity equation must appear as the source terms $S_i \boldsymbol{v}_i$ in the conservative form of the momentum equation for each species. To account for the source terms in both the continuity and momentum equations, the transport step can be split into two substeps by applying the operator-splitting technique.

Appendix B
Stability and Convergence of the Implicit Scheme

In Section 2, we addressed the stability and convergence of the implicit scheme based on the fact that $\boldsymbol{T}^{-1}$ exists, it is diagonalizable, strictly positive, and right stochastic. In this appendix, we demonstrate these properties.

B.1. $\boldsymbol{T}$ is Nonsingular

To show that $\boldsymbol{T}$ is nonsingular, it is enough to prove that zero is not an eigenvalue of it. We first note that, if λ_T is an eigenvalue of $\boldsymbol{T} = \boldsymbol{I} + \Delta t \boldsymbol{M}$, then $\lambda_M = (\lambda_T - 1)/\Delta t$ is an eigenvalue of $\boldsymbol{M}$. Upper and lower bounds for λ_M can be found by means of the Gershgorin circle theorem which, from Equation (11), implies

$$0 \leqslant \lambda_M \leqslant 2 \max_{k=1,\ldots,N} \left(\sum_{j \neq k}^{N} \alpha_{kj} \right). \tag{90}$$

Hence, all the eigenvalues of $\boldsymbol{M}$ are real and nonnegative. Because

$$\sum_{k=1}^{N} \boldsymbol{M}_{ik} = 0 \quad \text{for every } i = 1, \ldots, N, \tag{91}$$

$\lambda_M = 0$ is an eigenvalue and $\boldsymbol{M}$ is singular. We then conclude that $\lambda_T \geqslant 1$ provided $\Delta t > 0$.

B.2. $\boldsymbol{T}^{-1}$ is Diagonalizable

Because $\boldsymbol{M}$ and $\boldsymbol{T}$ commute, they are simultaneously diagonalizable. Therefore, to prove that $\boldsymbol{T}^{-1}$ is diagonalizable, it is enough to show that $\boldsymbol{M}$ is similar to a (real) symmetric matrix, i.e., $\boldsymbol{S} = \boldsymbol{D}^{-1}\boldsymbol{M}\boldsymbol{D}$ with $\boldsymbol{S} = \boldsymbol{S}^{\mathsf{T}}$. We demonstrate this as follows. Defining the diagonal matrix, $\boldsymbol{R}$, with elements $R_{ij} = \rho_i/\rho_0 \delta_{ij}$, for any arbitrary ρ_0 and $i, j = 1, \ldots N$, Equation (4) implies $R_{ik} M_{kj} = R_{jk} M_{ki}$, i.e., $\boldsymbol{R}\boldsymbol{M} = (\boldsymbol{R}\boldsymbol{M})^{\mathsf{T}}$ is symmetric. Because $\boldsymbol{R}$ is diagonal, it follows that $\boldsymbol{R}\boldsymbol{M} = \boldsymbol{M}^{\mathsf{T}}\boldsymbol{R}$. Multiplying this last equality, to both left and right, by the matrix $\boldsymbol{R}^{-1/2}$, we obtain $\boldsymbol{R}^{1/2}\boldsymbol{M}\boldsymbol{R}^{-1/2} = \boldsymbol{R}^{-1/2}\boldsymbol{M}^{\mathsf{T}}\boldsymbol{R}^{1/2} = (\boldsymbol{R}^{1/2}\boldsymbol{M}\boldsymbol{R}^{-1/2})^{\mathsf{T}}$. This demonstrates that the matrix $\boldsymbol{S} = \boldsymbol{D}^{-1}\boldsymbol{M}\boldsymbol{D}$ with $\boldsymbol{D} = \boldsymbol{R}^{-1/2}$ is symmetric.

B.3. $\boldsymbol{T}^{-1}$ is Right Stochastic

A right stochastic matrix is defined as a matrix whose entries are nonnegative and with each row summing to one.

From Equation (11), it is clear that

$$\sum_{j=1}^{N} \boldsymbol{T}_{ij} = 1 + \Delta t \sum_{j=1}^{N} \boldsymbol{M}_{ij} = 1, \tag{92}$$

and because $\sum_j \sum_k T_{ik} T^{-1}_{kj} = \sum_j \delta_{ij}$, $\sum_j \boldsymbol{T}^{-1}_{ij} = 1$. Furthermore,

$$\boldsymbol{T}_{ij} < 0, \quad \text{for } i \neq j, \tag{93}$$

so $\boldsymbol{T}$ belongs to the group of matrices $\mathbb{Z}^{n \times n}$. In addition, because the eigenvalues of $\boldsymbol{T}$ are real and positive (see Appendix B.1), $\boldsymbol{T}$ is a nonsingular $\mathbb{M}$ matrix (see Theorem 2.3, chapter 6, Berman & Plemmons 1979) and $\boldsymbol{T}$ has a nonnegative inverse.

B.4. $\boldsymbol{T}^{-1}$ is Strictly Positive

The inverse, $\boldsymbol{T}^{-1}$, of an irreducible nonsingular $\mathbb{M}$ matrix is strictly positive (see Theorem 2.7, chapter 6, Berman & Plemmons 1979), i.e., $\boldsymbol{T}^{-1}_{i,j} > 0$ for all $i, j \in 1 \ldots N$. Because $\boldsymbol{T}$ is a nonsingular $\mathbb{M}$ matrix (see Appendix B.3), it only remains to be demonstrated that $\boldsymbol{T}$ is irreducible.

Theorem 2.7 (chapter 2) from Berman & Plemmons (1979) states that a matrix $\boldsymbol{T}$ is irreducible if and only if its direct graph, $G(\boldsymbol{T})$, is strongly connected. $G(\boldsymbol{T})$ consists of n vertices $P_1, \cdots, P_n$, where an edge leads from P_i to P_j if and only if $T_{ij} \neq 0$. Furthermore, it is strongly connected if, for any ordered pair (P_i, P_j) of vertices, there exists a path that leads from P_i to P_j. Clearly, if all species collide with each other, then $T_{ij} \neq 0$ for all i, j and $G(\boldsymbol{T})$ is strongly connected. This statement holds, even when ignoring direct collisions between species i and j, provided that each species collides with another (proxy) species k. This is because the path from P_i to P_j is defined through P_k.

Appendix C
Nonlinear Drag Force

The collision rate might depend on the relative velocity between species, Δv, and Equations (5) become nonlinear in the velocities. Because the implicit scheme described by Equation (6) assumes a linear system, in principle, it cannot be used to find the solution in such a nonlinear regime. In this appendix, we present simple tests of an approximation that allows us to circumvent this issue, which consists in assuming the system to be linear in Δv^{n+1}, and the collision rate, α^n, to be dependent on Δv^n. This approximation makes it possible for all the properties of the implicit scheme to hold even in the nonlinear drag regime. By means of a simple example, we show that this method is good enough to recover the solution of Equations (5) in the nonlinear regime. For this test, we adopt the three different collision rates presented in Table 6.

Table 6
Collision Rate α for the different Nonlinear Drag Force Laws Showed in Figure 12

Linear	Quadratic	Power Law	Mixed
γ	$\gamma_q\lvert\Delta v\rvert$	$\gamma_p\lvert\Delta v\rvert^{1/p}$	$\gamma_m\sqrt{1+b_m\lvert\Delta v\rvert^2}$

Note. The coefficients γ, γ_q, γ_p, γ_m, and b_m are all fixed to one for the purpose of this test.

We consider two species with initial densities and velocities, $\rho_1 = \rho_2 = 1$ and $v_1 = 20$, $v_2 = 10$, respectively, and obtain numerical solutions following Section 3.1. For the power-law regime, we set the index $p = 2$.

In each panel of Figure 12 we show the analytical and numerical solutions with solid lines and unfilled circles, respectively. The dashed lines correspond to the solution obtained for a linear drag force. In all nonlinear drag regimes, the agreement between the analytical and numerical solutions is excellent.

Appendix D
Eigenvalues for the Sound Wave Test Problem

To solve the dispersion relation (45), we write it as the polynomial equation

$$P(\omega) = \omega^{N+1} + a_N\omega^N + \cdots + a_0 = 0. \tag{94}$$

The $N+1$ roots of Equation (94) are the eigenvalues of the problem. The polynomial P has at least $N-1$ real positive roots. This is proved by first noticing that F is positive for $\omega < \min(t_{sm}^{-1})$. Because $t_{sm} > 0$, no real root exists for $\omega < 0$. In addition, the one-sided limits of F satisfy

$$\lim_{\omega\to t_{sm}^{-1\pm}} F(\omega, \omega_s) = \pm\infty, \tag{95}$$

i.e., the function changes sign at each side of the singular points, from which we conclude that there is at least one real positive root between two adjacent singular points, giving $N-2$ positive roots. Furthermore, because

$$\lim_{\omega\to\infty} F(\omega, \omega_s) = \infty, \tag{96}$$

there is at least one more positive root beyond the last singular point. All of these roots correspond to pure damping solutions.

An upper bound for the largest real root can found. Defining t_{sN-1}^{-1} as the largest singular point, for $\omega \gg t_{sN-1}^{-1}$, $f > 0$ if

$$1 + \sum_{m=1}^{N-1}\frac{\epsilon_m}{1-\omega t_{sm}} \simeq 1 - \frac{1}{\omega}\sum_{m=1}^{N-2}\frac{\epsilon_m}{t_{sm}} + \frac{\epsilon_{N-1}}{1-\omega t_{sN-1}} > 0. \tag{97}$$

This expression is equivalent to the quadratic inequality

$$-t_{sN-1}\omega^2 + \left[1 + \epsilon_{N-1} + t_{sN-1}\sum_{m=1}^{N-2}\frac{\epsilon_m}{t_{sm}}\right]\omega - \sum_{m=1}^{N-2}\frac{\epsilon_m}{t_{sm}} > 0, \tag{98}$$

from which we find that the largest positive root of P is smaller than the largest root of Equation (98).

Having found the $N-1$ roots of P, $\{\omega_1, \ldots, \omega_{N-1}\}$, we can use Vieta's formulae to find the remaining roots ω_N and ω_{N+1},

$$\omega_N\omega_{N+1} = (-1)^{N+1}a_0\prod_{j=1}^{N-1}\omega_j^{-1}, \tag{99}$$

$$\omega_N + \omega_{N+1} = -a_N - \sum_{j=1}^{N-1}\omega_j, \tag{100}$$

where a_0, a_N are

$$a_0 = (-1)^{N-1}\omega_s^2\prod_{j=1}^{N-1}t_{sj}^{-1}, \tag{101}$$

$$a_N = -\sum_{j=1}^{N-1}t_{sj}^{-1}(1+\epsilon_j). \tag{102}$$

Equations (99)–(100) can be written as a second-order polynomial equation, from which we obtain the final two roots, which are, in general, complex and are the most interesting ones.

Appendix E
Equations for the Streaming Instability

We linearize Equations (75)–(78) around the background solutions, Equations (81)–(84). Without loss of generality, we assume perturbations of the form $\delta f = \delta\hat{f}\, e^{i(k_x x + k_z z)-\omega t}$. Defining the dimensionless densities $\delta\tilde{\rho} = \delta\hat{\rho}/\rho_g^0$ and $\epsilon_k^0 = \rho_k^0/\rho_g^0$, velocities $\tilde{v} = \hat{v}/(h_0^2 v_{K0})$, wavenumber $K = kh_0^2 v_{K0}/\Omega_0$, eigenvalue $\tilde{\omega} = \omega/\Omega_0$, and relative velocities $\Delta_{kx}^0 = \tilde{v}_{gx}^0 - \tilde{v}_{kx}^0$, $\Delta_{ky}^0 = \tilde{v}_{gy}^0 - \tilde{v}_{ky}^0$, the equations describing the linear evolution of the system are

$$iK_x\tilde{v}_{gx}^0\delta\tilde{\rho}_g + iK_x\delta\tilde{v}_{gx} + iK_z\delta\tilde{v}_{gz} = \tilde{\omega}\delta\tilde{\rho}_g \tag{103}$$

$$\left(iK_x h_0^{-2} - \sum_{k=1}^{N}\frac{\epsilon_k^0\Delta_{kx}^0}{T_{sk}}\right)\delta\tilde{\rho}_g + \left(iK_x\tilde{v}_{gx}^0 + \sum_{k=1}^{N}\frac{\epsilon_k^0}{T_{sk}}\right)\delta\tilde{v}_{gx} - 2\delta\tilde{v}_{gy} + \sum_{k=1}^{N}\frac{\Delta_{kx}^0}{T_{sk}}\delta\tilde{\rho}_k - \sum_{k=1}^{N}\frac{\epsilon_k^0}{T_{sk}}\delta\tilde{v}_{kx} = \tilde{\omega}\delta\tilde{v}_{gx} \tag{104}$$

$$-\left(\sum_{k=1}^{N}\frac{\epsilon_k^0\Delta_{ky}^0}{T_{sk}}\right)\delta\tilde{\rho}_g + (2-q)\delta\tilde{v}_{gx} + \left(iK_x\tilde{v}_{gx}^0 + \sum_{k=1}^{N}\frac{\epsilon_k^0}{T_{sk}}\right)\delta\tilde{v}_{gy} + \sum_{k=1}^{N}\frac{\Delta_{ky}^0}{T_{sk}}\delta\tilde{\rho}_k - \sum_{k=1}^{N}\frac{\epsilon_k^0}{T_{sk}}\delta\tilde{v}_{ky} = \tilde{\omega}\delta\tilde{v}_{gy} \tag{105}$$

$$iK_z h_0^{-2}\delta\tilde{\rho}_g + \left(iK_x\tilde{v}_{gx}^0 + \sum_{k=1}^{N}\frac{\epsilon_k^0}{T_{sk}}\right)\delta\tilde{v}_{gz} - \sum_{k=1}^{N}\frac{\epsilon_k^0}{T_{sk}}\delta\tilde{v}_{kz} = \tilde{\omega}\delta\tilde{v}_{gz} \tag{106}$$

$$iK_x\tilde{v}_{jx}^0\delta\tilde{\rho}_j + iK_x\epsilon_j^0\delta\tilde{v}_{jx} + iK_z\epsilon_j^0\delta\tilde{v}_{jz} = \tilde{\omega}\delta\tilde{\rho}_j \tag{107}$$

$$-\frac{1}{T_{sj}}\delta\tilde{v}_{gx} + \left(iK_x\tilde{v}_{jx}^0 + \frac{1}{T_{sj}}\right)\delta\tilde{v}_{jx} - 2\delta\tilde{v}_{jy} = \tilde{\omega}\delta\tilde{v}_{jx} \tag{108}$$

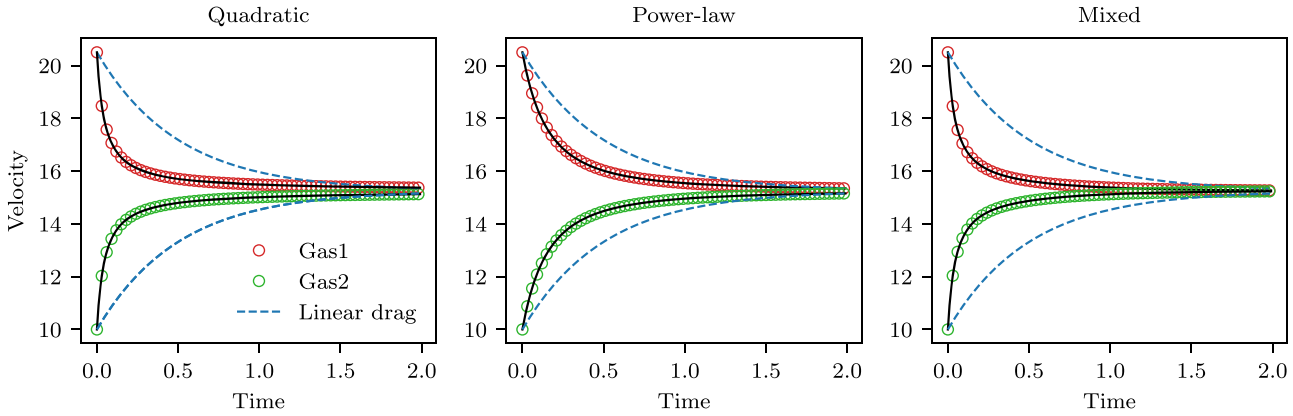

Figure 12. Analytical (solid lines) and numerical (unfilled circles) solutions for a quadratic (left panel), power law with $p = 2$ (center panel), and mixed (right panel) drag forces. The dashed line is the solution for a linear drag force.

$$-\frac{1}{T_{sj}}\delta\tilde{v}_{gy} + (2-q)\delta\tilde{v}_{jx} + \left(iK_x\tilde{v}^0_{jx} + \frac{1}{T_{sj}}\right)\delta\tilde{v}_{jy} = \tilde{\omega}\delta\tilde{v}_{jy} \quad (109)$$

$$-\frac{1}{T_{sj}}\delta\tilde{v}_{gz} + \left(iK_x\tilde{v}^0_{jx} + \frac{1}{T_{sj}}\right)\delta\tilde{v}_{jz} = \tilde{\omega}\delta\tilde{v}_{jz}. \quad (110)$$

References

Bai, X.-N., & Stone, J. M. 2010, ApJS, 190, 297
Balsara, D. S., Tilley, D. A., Rettig, T., & Brittain, S. D. 2009, MNRAS, 397, 24
Barge, P., & Sommeria, J. 1995, A&A, 295, L1
Baruteau, C., & Zhu, Z. 2016, MNRAS, 458, 3927
Benítez-Llambay, P., & Masset, F. S. 2016, ApJS, 223, 11
Benítez-Llambay, P., & Pessah, M. E. 2018, ApJL, 855, L28
Benítez-Llambay, P., Ramos, X. S., Beaugé, C., & Masset, F. S. 2016, ApJ, 826, 13
Benilov, M. S. 1997, PhPl, 4, 521
Berman, A., & Plemmons, R. J. 1979, Nonnegative Matrices in the Mathematical Sciences (New York: Academic)
Béthune, W., Lesur, G., & Ferreira, J. 2016, A&A, 589, A87
Booth, R. A, Sijacki, D., & Clarke, C. J. 2015, MNRAS, 452, 3932
Braginskii, S. I. 1965, RvPP, 1, 205
Brandenburg, A., & Dobler, W. 2002, CoPhC, 147, 471
Chen, J.-W., & Lin, M.-K. 2018, MNRAS, 478, 2737
Chrenko, O., Brož, M., & Lambrechts, M. 2017, A&A, 606, A114
de Val-Borro, M., Edgar, R., Artymowicz, P., et al. 2006, MNRAS, 370, 529
Dipierro, G., & Laibe, G. 2017, MNRAS, 469, 1932
Dipierro, G., Laibe, G., Alexander, R., & Hutchison, M. 2018, MNRAS, 479, 4187
Drążkowska, J., Hanasz, M., & Kowalik, K. 2010, Particle Module of Piernik MHD Code, Astrophysics Source Code Library, ascl:1010.005
Fromang, S., & Papaloizou, J. 2006, A&A, 452, 751
Fung, J., Shi, J.-M., & Chiang, E. 2014, ApJ, 782, 88
Hanasz, M., Kowalik, K., Wóltański, D., Pawłaszek, R., & Kornet, K. 2010, in EAS Publications Series 42, ed. K. Goździewski, A. Niedzielski, & J. Schneider (Les Ulis: EAS), 281
Hawley, J. F., Smarr, L. L., & Wilson, J. R. 1984, ApJS, 55, 211
Hunter, J. D. 2007, CSE, 9, 90
Hutchison, M., Price, D. J., & Laibe, G. 2018, MNRAS, 476, 2186
Johansen, A., Andersen, A. C., & Brandenburg, A. 2004, A&A, 417, 361
Johansen, A., & Youdin, A. 2007, ApJ, 662, 627
Kowalik, K., Hanasz, M., Wóltański, D., & Gawryszczak, A. 2013, MNRAS, 434, 1460
Krapp, L., Gressel, O., Benítez-Llambay, P., et al. 2018, ApJ, 865, 105
Laibe, G., & Price, D. J. 2011, MNRAS, 418, 1491
Laibe, G., & Price, D. J. 2012, MNRAS, 420, 2345
Laibe, G., & Price, D. J. 2014, MNRAS, 444, 1940
Lehmann, A., & Wardle, M. 2018, MNRAS, 476, 3185
Lyra, W., & Lin, M.-K. 2013, ApJ, 775, 17
Miniati, F. 2010, JCoPh, 229, 3916
Nakagawa, Y., Sekiya, M., & Hayashi, C. 1986, Icar, 67, 375
Paardekooper, S.-J., & Mellema, G. 2006, A&A, 453, 1129
Pérez, F., & Granger, B. E. 2007, CSE, 9, 21
Porth, O., Xia, C., Hendrix, T., Moschou, S. P., & Keppens, R. 2014, ApJS, 214, 4
Press, W. H., Teukolsky, S. A., Vetterling, W. T., & Flannery, B. P. 2007, Numerical Recipes 3rd Edition: The Art of Scientific Computing (3rd ed.; New York: Cambridge Univ. Press)
Price, D. J., Wurster, J., Tricco, T. S., et al. 2018, PASA, 35, e031
Ragusa, E., Dipierro, G., Lodato, G., Laibe, G., & Price, D. J. 2017, MNRAS, 464, 1449
Riols, A., & Lesur, G. 2018, A&A, 617, A117
Safronov, V. S. 1972, Evolution of the Protoplanetary Cloud and Formation of the Earth and Planets (Jerusalem: Keter Publishing House)
Stone, J., Gardiner, T., Teuben, P., Hawley, J., & Simon, J. 2008, ApJS, 178, 137
Stone, J., & Norman, M. 1992, ApJS, 80, 753
Stone, J. M. 1997, ApJ, 487, 271
Stoyanovskaya, O. P., Glushko, T. A., Snytnikov, N. V., & Snytnikov, V. N. 2018, A&C, 25, 25
Stoyanovskaya, O. P., Vorobyov, E. I., & Snytnikov, V. N. 2018, ARep, 62, 455
van der Walt, S., Colbert, S. C., & Varoquaux, G. 2011, CSE, 13, 22
Vorobyov, E. I., Akimkin, V., Stoyanovskaya, O., Pavlyuchenkov, Y., & Liu, H. B. 2018, A&A, 614, A98
Weber, P., Benítez-Llambay, P., Gressel, O., Krapp, L., & Pessah, M. 2018, ApJ, 854, 153
Weidenschilling, S. J. 1977, MNRAS, 180, 57
Whipple, F. L. 1972, in From Plasma to Planet, ed. A. Elvius (New York: Wiley), 211
Yang, C.-C., & Johansen, A. 2016, ApJS, 224, 39
Youdin, A., & Johansen, A. 2007, ApJ, 662, 613
Youdin, A. N., & Goodman, J. 2005, ApJ, 620, 459
Zhu, Z., & Stone, J. M. 2014, ApJ, 795, 53